Mergers of black-hole binaries with aligned spins: Waveform characteristics

Bernard J. Kelly,[1,2] John G. Baker,[3] William D. Boggs,[4] Sean T. McWilliams,[5,6] and Joan Centrella[3]

[1]*CRESST and Gravitational Astrophysics Laboratory, NASA Goddard Space Flight Center,*
8800 Greenbelt Road, Greenbelt, Maryland 20771, USA
[2]*Department of Physics, University of Maryland, Baltimore County, 1000 Hilltop Circle, Baltimore, Maryland 21250, USA*
[3]*Gravitational Astrophysics Laboratory, NASA Goddard Space Flight Center, 8800 Greenbelt Road, Greenbelt, Maryland 20771, USA*
[4]*Department of Physics, University of Maryland, College Park, Maryland 20742, USA*
[5]*Institute for Strings, Cosmology, and Astroparticle Physics (ISCAP), Columbia University, New York, New York 10027, USA*
[6]*Department of Physics, Princeton University, Princeton, New Jersey 08544, USA*

We conduct a descriptive analysis of the multipolar structure of gravitational-radiation waveforms from equal-mass aligned-spin mergers, following an approach first presented in the complementary context of nonspinning black holes of varying mass ratio [J. G. Baker *et al.*, Phys. Rev. D **78**, 044046 (2008).]. We find that, as with the nonspinning mergers, the dominant waveform mode phases evolve together in lock-step through inspiral and merger, supporting the previous waveform description in terms of an adiabatically rigid rotator driving gravitational-wave emission—an *implicit rotating source*. We further apply the late-time merger-ringdown model for the *rotational frequency* introduced in [J. G. Baker *et al.*, Phys. Rev. D **78**, 044046 (2008).], along with an improved amplitude model appropriate for the dominant $(2, \pm 2)$ modes. This provides a quantitative description of the merger-ringdown waveforms, and suggests that the major features of these waveforms can be described with reference only to the intrinsic parameters associated with the state of the final black hole formed in the merger. We provide an explicit model for the merger-ringdown radiation, and demonstrate that this model agrees to fitting factors better than 95% with the original numerical waveforms for system masses above $\sim 150 M_\odot$. This model may be directly applicable to gravitational-wave detection of intermediate-mass black-hole mergers.

I. INTRODUCTION

Black-hole-binary mergers are a key target of ground-based and space-based gravitational-wave observations. The strongest radiation is produced just as the two black holes join to become one, and can only be fully understood through explicit numerical simulations. Since the first stable evolutions of black-hole-binary mergers [1–4], and after it was established that the gravitational waveforms from these evolutions were universal, and consistent across codes and methodologies [5–7], researchers have turned their attention to how the results of numerical relativity can most usefully be supplied to the gravitational-wave data-analysis community.

After studying the equal-mass nonspinning case, researchers have had to address the complexity problem of more generic systems. Even allowing for simple scaling by total mass $M = M_1 + M_2$, and assuming zero eccentricity, such systems span a seven-dimensional parameter space: $\{\eta, \vec{S}_1, \vec{S}_2\}$, where $\eta = M_1 M_2 / M^2$ is the *symmetric mass ratio* of the binary, and $\vec{S}_i$ is the spin angular momentum vector of hole i.

Early surveys of the waveform parameter space have restricted themselves to the η-dependence of nonspinning systems. In [8], the authors investigated the multipole structure of merger waveforms from such systems, noting that the strongest subdominant modes shared many

characteristics with the dominant quadrupole, and that they could be collectively described by an *implicit rotating source* model of the binary. The authors used this observation to construct a multimode gravitational-wave template family for such binary systems, as an alternative to more usual effective-one-body (EOB) templates [9,10].

While we may assume that η and $|\vec{S}_i|$ remain essentially constant throughout inspiral and merger, the spin directions generally evolve, so a useful parametrization of the system should take care to distinguish components of the spin-direction space with physically distinct effects on the waveforms [11].

An obvious cut in parameter space to consider is that of spins aligned (or antialigned) with the orbital angular momentum. These systems will not precess, but exhibit observationally significant spin-orbit effects, distinguishing them from nonspinning binaries in their dynamics and resulting waveforms [12]. High-accuracy waveforms from such evolutions have been produced and studied by several groups [13–16]. Such systems have been partially characterized by [17], using a variant of the frequency model from [8]. The frequency-domain phenomenological templates of Ajith *et al.* have been extended to cover both mass ratio and total aligned spin [18,19], at least for the dominant modes, and attempts have been made to extend these to more generic systems [20,21].

A key result from our investigation of the dominant modes of nonspinning unequal-mass binary waveforms [8] was that these modes had phases that evolved together in lock-step through inspiral and merger. This agreement was especially impressive for the $\ell = m$ modes, leading to the development of a heuristic picture of the binary system as a rigid rotator (at least in the adiabatic limit) driving gravitational-wave emission. We dubbed this the *implicit rotating source* (IRS) picture.

A secondary result of this picture was the possibility of developing a simple model for the time-development of the dominant and leading subdominant modal frequencies $\omega_{\ell m}$ in terms of a single *rotational frequency* $\Omega(t)$:

$$\omega_{\ell m} = m\Omega(t).$$

We also presented a simple model for the corresponding mode amplitudes, leading to the possibility of a new approach to time-based gravitational-waveform templates. In fact, we developed such a template proposal, the IRS-EOB templates, as an alternative to the effective-one-body templates of [9,10], which terminate the signals by matching to a superposition of quasinormal-mode (QNM) frequencies.

In this paper, we look at the dominant waveform modes from some aligned-spin systems, and ask the following general questions: Does the general IRS picture still hold? How do the features of aligned-spin mergers compare with those of nonspinning mergers? Can we quantify the main features of the merger ringdown with a simple analytic model?

The rest of this paper is laid out as follows. In Sec. II, we introduce the binary systems studied and the numerical methods used to simulate them. In Sec. III, we present results for the final black-hole states and an IRS descriptive characterization of the waveforms from our numerical evolutions. In Sec. IV, we analyze the late portions of these waveforms in more detail, and apply the analytic modeling approach of [8] to the dominant-mode frequencies and (with improvements) to the amplitude model, concluding with an explicit parametrization approximating the (2, 2) results of all our simulations. In Sec. V, we investigate the quality of the new models compared to the numerical waveforms in the context of the Advanced LIGO detector.

We conclude with some discussion in Sec. VI. Some extra detail on the convergence of the numerical simulations is given in the Appendix.

II. SIMULATIONS

To investigate the nature of aligned-spin binary waveforms, we carried out a series of numerical evolutions for equal-mass systems with zero spin (X100), spins aligned with the initial orbital angular momentum (X1UU), anti-aligned (X1DD), or mixed (X1UD). We also reran, for purposes of comparison, the case of a 4:1 nonspinning binary (X400).

The physical parameters of these evolutions are presented in Table I. The initial momenta of the equal-mass binaries, with the exception of X1UU, were chosen by integrating the post-Newtonian equations of motion, as outlined in [22,23], with spin contributions to the Hamiltonian adapted from [24–28] (although we work in the Arnowitt-Deser-Misner (ADM) gauge, the results from harmonic gauge using effective-field theory [26] have been shown to be equivalent [29,30]), and the flux from [31]. For the X1UU configuration, we used simpler quasicircular initial parameters with no initial ingoing radial momentum. For the X400 data, we retained the quasicircular initial parameters used in [8].

The equal-mass runs were carried out with our HAHNDOL evolution code [32] using the PARAMESH mesh-refinement infrastructure [33]. The new X400 data, however, use HAHNDOL paired with the Einstein Toolkit [34] release of the Cactus Computational Toolkit [35] and the CARPET mesh-refinement driver [36].

In all cases, the initial data are of the standard Brandt-Brügmann type [37], using the Bowen-York [38] prescription for extrinsic curvature that exactly satisfies the momentum constraint. We solve the remaining Hamiltonian constraint using the TWOPUNCTURES spectral code [39]. This code also supplies the total ADM energy M_{ADM} of the system, as well as the individual "puncture ADM masses" $M_{\text{ADM},i}$, to very high precision. We note, however, that for highly spinning or boosted Bowen-York-type data, a measurable amount of radiation energy may be included

TABLE I. Physical and numerical parameters of the initial data for all the runs presented. $m_{1,p}$ and $m_{2,p}$ are the bare puncture masses of the two premerger holes. r_0 and P_0 are the initial coordinate separation and (transverse) linear momentum, respectively, giving rise to a total initial orbital angular momentum L_0. M_{ADM} is the total energy of the initial data. The total infinite-separation total mass M of the system is estimated by M_{AH}, the sum of the initial (apparent) horizon masses of the two holes, calculated at $t = 100$. Finally, we quote the approximate observed eccentricity (1).

Run name	$m_{1,p} = m_{2,p}$	S_{1z}	S_{2z}	r_0	$P_{0t}(\times 10^2)$	$P_{0r}(\times 10^4)$	L_0	M_{ADM}	$\sum_i M_{\text{ADM},i}$	M_{AH}	$e_{\Omega,\max}$
X100	0.4872312	0.0	0.0	11.0000	9.00993	7.09412	0.991092	0.990514	1.000050	1.000050	0.002
X1UU	0.301805	0.2	0.2	8.2013	10.3248	0.0	0.846768	0.988459	1.000908	1.000550	0.01
X1DD	0.390411	−0.159125	−0.159125	11.9837	8.83600	1.20000	1.058879	0.990453	0.998794	0.998686	0.01
X1UD	0.301805	0.2	−0.2	11.0000	9.00993	7.09412	0.991092	0.990024	0.999222	0.998834	0.002
X400	0.7900, 0.1890	0.0	0.0	8.4702	6.95662	0.0	0.589240	0.992912	1.000310	1.000315	0.02

in these puncture ADM masses, but then escape to infinity [7,40–42]; thus the initial puncture ADM mass may not be the optimal measure of premerger black-hole mass. These quantities are also listed in Table I.

To evolve these initial data, we employ the BSSNOK $3 + 1$ decomposition of Einstein's vacuum equations [43–45], with the alternative conformal variable suggested in [46–48], constraint-damping terms suggested in [49], and the dissipation terms suggested in [50,51]. Our gauge conditions are the specific $1 + \log$ lapse and gamma-driver shift described in [52], which constitute a variant of the now-standard "moving punctures" approach [3,4].

The four equal-mass simulations—X100, X1UU, X1DD, and X1UD—were conducted with the HAHNDOL/PARAMESH version of our code using space-only adaptive mesh-refinement (AMR) with grids placed adaptively, based on curvature invariants [5]. The 4:1 mass-ratio simulation X400 was carried out with the same evolution routines, now ported to run within Cactus/CARPET [34–36], which applies mesh-refinement in time as well as in space. The initial grid structures for all runs are given in Table II. For the equal-mass simulations, the highest-resolution regions closest to the punctures had a grid spacing of $3M/160$, $M/64$, or $3M/224$ for the medium-, high-, and ultrahigh-resolution evolutions (the ultrahigh was performed for X1UD only). For the X400 simulation, the grid resolution around the smaller hole was $M/96$, $M/128$, and $M/160$ for the medium-, high-, and ultrahigh-resolution runs.

The equal-mass simulations exhibit between second- and fifth-order convergence for the Hamiltonian constraint, while the momentum constraints only showed clear second-order convergence in the highest-resolution regions around the punctures. Nevertheless, waveform amplitudes and phases were sixth-order convergent over the majority of the evolution. The remaining simulation, X400, displays sixth-order convergence in waveform amplitude and phase until close to merger time. For details, we refer the reader to the Appendix.

We use the AHFINDERDIRECT code [53,54] to locate the individual holes, as well as the final post-merger hole. We deduce the horizon mass from the horizon area A_{AH} via Christodoulou's relation [55]

$$M_{\mathrm{AH}}^2 = M_{\mathrm{irr}}^2 + \frac{J^2}{4M_{\mathrm{irr}}^2},$$

where $M_{\mathrm{irr}} = \sqrt{A_{\mathrm{AH}}/16\pi}$ is the *irreducible mass* of the hole. We present the sum of the two horizon masses, $M_{\mathrm{AH}} \equiv M_{\mathrm{AH},1} + M_{\mathrm{AH},2}$ in Table I, and use it for time-scaling of gravitational waveforms.

Following [22,56], we estimate eccentricity using the variation in puncture orbital frequency Ω_{punc}:

$$e_\Omega(t) \equiv \frac{(\Omega_{\mathrm{punc}} - \Omega_{\mathrm{circ}})}{2\Omega_{\mathrm{circ}}}, \qquad (1)$$

where Ω_{circ} is a monotonic fit to Ω_{punc}, based on a simple post-Newtonian expansion. For a good fitting function, the residual $e_\Omega(t)$ should be a sinusoid of slowly decreasing amplitude, and period equal to the orbital period; the eccentricity is then the (nearly constant) amplitude, $e_{\Omega,\mathrm{max}}$. In practice, due in part to gauge-dependent behavior in the puncture tracks, $e_\Omega(t)$ is not perfectly sinusoidal. Nevertheless, we quote the derived eccentricity measure for each run in Table I. This is higher than we would like for serious data-analysis applications, or for generating post-Newtonian–numerical-relativity hybrid waveforms, and we could choose to reduce eccentricity through methods similar to those presented in [17]. However, our primary purpose in this paper is to investigate the bulk behavior of the waveform modes across configurations, and very low eccentricity does not appear to be necessary for this.

To obtain gravitational waveforms from our simulations, we begin by calculating the "outgoing radiation" Weyl scalar ψ_4 [57], corresponding to the tidal accelerations that are to be measured by gravitational-wave instruments. ψ_4 is a complex quantity related to the wave strain $h = h_+ + ih_\times$ by two time-derivatives: $\psi_4 = -\ddot{h}_+ + i\ddot{h}_\times$ [58]. We interpolate ψ_4 onto a set of coordinate spheres, and decompose the values on these spheres into spherical harmonics of spin-weight $s = -2$, $-2Y_\ell^m$:

$$r\psi_4(t, r, \theta, \phi) = \sum_{\ell m} C_{\ell m}(t, r)_{-2}Y_\ell^m(\theta, \phi).$$

To obtain the harmonic modes of the strain h, therefore, we must integrate $C_{\ell m}(t, r)$ twice in time, with integration constants taken to yield zero strain long after the merger has taken place; we call this process "detrending" the waveform. Currently, we use the Fourier-domain method of time-integration presented in [59] to produce a strain

TABLE II. Initial grid structure of the different simulations. The left-most number is the outer extent of the Cartesian grid, with resolution doubled (grid spacing halved) within each new refinement level.

Run name	Outer (fixed) grid structure	Inner (moving) grid structure
X100, X1DD, X1UD	[1536, 768 384 192, 144, 72, 24, 12, 8]	[3.0, 1.5, 0.75]
X1UU	[1536, 768, 384, 192, 96, 72, 24, 12, 8]	[3.0, 1.5, 0.75]
X400 (larger puncture)	[2048, 1024, 512, 256, 160, 96]	[20, 10, 5, 2.75, 1.5]
X400 (smaller puncture)	[2048, 1024, 512, 256, 160, 96]	[20, 10, 5, 2.5, 1.25, 0.6875, 0.375]

waveform h that is free of unwanted secular trends. This can also be written as a sum over modes:

$$rh(t, r, \theta, \phi) = \sum_{\ell m} H_{\ell m}(t, r) e^{i\varphi^h_{\ell m}(t, r)}{}_{-2}Y^m_\ell(\theta, \phi). \quad (2)$$

In fact, we are most interested in an intermediate quantity, $\dot{h}$, which we call the *strain-rate*. This is of particular interest because it is most closely related to the rates of emission of gravitational-wave energy and linear momentum [60,61]. As with the strain and ψ_4, the strain-rate can be decomposed into spherical harmonics:

$$r\dot{h}(t, r, \theta, \phi) = \sum_{\ell m} A_{\ell m}(t, r) e^{i(\varphi_{\ell m}(t, r) + \pi/2)}{}_{-2}Y^m_\ell(\theta, \phi), \quad (3)$$

where we have explicitly included a phase offset $\pi/2$ so that the remaining strain-rate phase $\varphi_{\ell m}$ differs from the strain phase $\varphi^h_{\ell m}$ only by terms of 2.5PN order (see discussion in [57]).

For the equal-mass cases, our extraction spheres were $r_{\text{ext}} \in \{45M, 50M, 55M, 60M, 65M, 70M\}$, with a consistent extraction-region resolution of $6M/5$, M, and $4M/5$ for central resolutions of $3M/160$, $M/64$, and $3M/224$, respectively. For the X400 case, the spheres were $r_{\text{ext}} \in \{40M, 50M, 60M, 70M, 80M, 90M\}$. In these regions, the extraction-region resolution was M and $4M/5$ for central resolutions of $M/128$ and $M/160$, respectively.

In addition to errors in the strong-field region of the source, the extracted waveforms will also contain errors due both to finite extraction radius and finite grid resolution in the extraction region. To mitigate the former, we have applied an extrapolation scheme to both waveform amplitude and waveform phase. Specifically, we assume a falloff model

$$A_{r_{\text{ext}}} = A_\infty + \frac{a_2}{r^2_{\text{ext}}}, \qquad \varphi_{r_{\text{ext}}} = \varphi_\infty + \frac{f_2}{r^2_{\text{ext}}}. \quad (4)$$

Of all two-parameter r_{ext}-falloff models we have tried, this model gives the best fit to the amplitude and phase of the dominant $(2, \pm 2)$ modes. Adding more terms to the falloff model will introduce overfitting errors, especially given the limited range of our r_{ext} domain. This leading-order behavior is consistent with r_{ext}-falloff predictions of [62]. This model, however, seems inappropriate for higher-frequency modes such as $(4, \pm 4)$, where dissipation effects cause a general loss in amplitude. For these, we include the possibility of an additional term proportional to r_{ext}, at least for the amplitude:

$$A_{r_{\text{ext}}} = a_{-1} r_{\text{ext}} + A_\infty + \frac{a_2}{r^2_{\text{ext}}}. \quad (5)$$

We use this model for all modes with $m > 3$. We note, however, that diffusive effects should only act to *decrease* the amplitude. If a mode shows apparent *growth* that does

not converge with some inverse power of r_{ext}, then it cannot be meaningfully extrapolated according to (5).

III. DESCRIPTIVE RADIATION CHARACTERIZATION

As noted, the main objective of this paper is to characterize gravitational waveforms from aligned-spin mergers. In this section we present the main features of the radiation, in a spherical-harmonic modal decomposition. Our analysis follows the same approach developed in [8], which descriptively characterized the radiation from nonspinning mergers in terms of an *implicit rotating source*. In this approach, each modal waveform component is viewed as the trace of the dynamic development of one of a superposed set of source moments. To a very good approximation, each mode's radiation is circularly polarized, indicating rotational motion. This is registered in the waveform's *rotational phase* $\Phi_{\ell m} \equiv \varphi_{\ell m}/m$, while the modal amplitudes heuristically indicate the relative contributions of the source moments.

Our goal is to build on the characterization of nonspinning mergers with additional details revealing the effects of aligned spins through the merger. We first characterize the raw content of the radiation in terms of energy and angular momentum, then comparatively examine how the modal amplitudes and rotation phases develop in time.

A. Radiated energy and angular momentum and final states

To calculate the rate of energy and angular momentum emission via gravitational radiation during merger and ringdown, we apply the following mode-summation formulas (see Appendix A of [8]):

$$\frac{dE}{dt} = \sum_{\ell m} \frac{A^2_{\ell m}}{16\pi}, \quad (6)$$

TABLE III. Radiated energy and z angular momentum from all merger processes, in units of the infinite-separation total mass estimated by M_{AH} (final column of Table I). The primary value is the r_{ext}-extrapolated value of the $\ell = 6$ mode-sum of the integrals at highest spatial resolution, while the quoted uncertainty is the linear sum of three contributions: the standard error for the fit parameter for the $\ell = 6$ mode-sum at the highest resolution; the difference between the $\ell = 4$ and $\ell = 6$ mode-sums at this resolution; the difference between the $\ell = 6$ mode-sum result for the highest and next-highest resolutions (for X400, the $\ell = 5$ mode-sum was used instead of $\ell = 6$).

Run name	$\Delta E_{\text{rad}}(M_{\text{AH}})$	$\Delta J_{z,\text{rad}}(M^2_{\text{AH}})$
X100	0.038547 ± 0.000244	0.367786 ± 0.001117
X1UU	0.075636 ± 0.001413	0.482665 ± 0.003874
X1DD	0.027240 ± 0.000219	0.293735 ± 0.001084
X1UD	0.039792 ± 0.000440	0.373655 ± 0.001581
X400	0.014437 ± 0.000104	0.136347 ± 0.000853

TABLE IV. End-state Kerr parameters (M, α) of post-merger holes. $M_{\mathrm{f,rad}}$ and α_{rad}, and associated uncertainties, are derived from radiation balance (9) and (10)—see Table III. $M_{\mathrm{f,AH}}$ and α_{AH} come from the AHFINDERDIRECT code [53,54] and the HAHNDOL spin calculator [63]; quoted uncertainties are a combination of the post-merger variability of the irreducible mass and spin and the difference between the measured mass and spin from the highest and second-highest resolutions. $M_{\mathrm{f,AEI}}(M_{\mathrm{AH}})$ and α_{AEI} use the numerically tuned formulas (13) and (11) due to [14,64,65]; quoted uncertainties here are due to uncertainty in the fitting coefficients (12) and (14).

Run name	$M_{\mathrm{f,rad}}(M_{\mathrm{AH}})$	α_{rad}	$M_{\mathrm{f,AH}}(M_{\mathrm{AH}})$	α_{AH}	$M_{\mathrm{f,AEI}}(M_{\mathrm{AH}})$	α_{AEI}
X100	0.9519 ± 0.0002	0.6878 ± 0.0013	0.95165 ± 0.00001	0.68644 ± 0.00001	0.9517 ± 0.0003	0.68646 ± 0.00004
X1UU	0.9123 ± 0.0014	0.9165 ± 0.0055	0.91164 ± 0.00013	0.90720 ± 0.00015	0.9144 ± 0.0008	0.9114 ± 0.0264
X1DD	0.9645 ± 0.0002	0.4825 ± 0.0012	0.96303 ± 0.00002	0.48140 ± 0.00012	0.9637 ± 0.0006	0.4794 ± 0.0256
X1UD	0.9514 ± 0.0004	0.6847 ± 0.0019	0.94996 ± 0.00001	0.68408 ± 0.00002	0.9517 ± 0.0003	0.6865 ± 0.0243
X400	0.9782 ± 0.0001	0.4726 ± 0.0009	N/A	N/A	N/A	0.4748 ± 0.0093

$$\frac{dJ_z}{dt} = \sum_{\ell m} \frac{|m|}{16\pi} A_{\ell m} H_{\ell m} \cos(\varphi_{\ell m} - \varphi_{\ell m}^h), \qquad (7)$$

where we terminate the mode-sums at $\ell = 6$ for the equal-mass cases, and $\ell = 5$ for X400. We integrate the result in time to obtain the total energy E_{rad} and angular momentum $J_{z,\mathrm{rad}}$ (x and y components are zero by symmetry) emitted during the evolution. In principle, these calculations could be performed with the full waveforms, rather than the (ℓ, m) modes. In practice, however, we only output the mode-decomposed waveforms for post-evolution analysis, and an accurate high-order time-integration of ψ_4 within the evolution code is difficult. Additionally, post-evolution analysis with the waveform modes allows us to better control unphysical high-frequency noise. Rather than directly summing and integrating the r_{ext}-extrapolated strains and strain-rates, we instead integrate the finite-r_{ext} energy fluxes, and extrapolate the result according to the three-parameter fit

$$\Delta E_{\mathrm{rad},r_{\mathrm{ext}}} = \Delta E_{\mathrm{rad},\infty} + \frac{e_2}{r_{\mathrm{ext}}^2} + \frac{e_4}{r_{\mathrm{ext}}^4}, \qquad (8)$$

and similarly for the radiated angular momentum, ΔJ_z. However, when dissipation effects are significant, as for the X1UU data, we must amend this assumption according to our model (5). Adding an r_{ext}-proportional term to the strain-rate amplitude will introduce several new terms to a quadratic-in-amplitude quantity like E_{rad}. However, since this many terms are impossible to fit credibly with only six extraction radii, we instead extrapolate the waveform modes first according to (4) (for $m < 4$) and (5) (for $m \geq 4$), and then perform a mode-sum of the result. The results are given in Table III.

Now we present our estimates of the final state of the post-merger Kerr holes, encoded in the two parameters M_{f} and $\alpha \equiv S_z/M_{\mathrm{f}}^2$. Our estimates are derived from a number of sources, and are tabulated in Table IV.

Most directly, the columns marked $M_{\mathrm{f,rad}}$ and α_{rad} are derived from simple conservation of energy and angular momentum:

$$M_{\mathrm{f,rad}} = M_{\mathrm{ADM}} - \Delta E_{\mathrm{rad}}, \qquad (9)$$

$$\alpha_{\mathrm{rad}} = \frac{J_0 - \Delta J_{z,\mathrm{rad}}}{M_{\mathrm{f,rad}}^2} = \frac{L_0 + S_{1z} + S_{2z} - \Delta J_{z,\mathrm{rad}}}{M_{\mathrm{f,rad}}^2}, \qquad (10)$$

where ΔE_{rad} and $\Delta J_{z,\mathrm{rad}}$ are taken from Table III, and the remaining quantities are as in Table I.

We can compare with an end-state model based on fits to a range of numerical mergers. One such model for final mass, appropriate for equal-mass systems, was given by [14][1]:

$$M_{\mathrm{f,AEI}}/M_{\mathrm{AH}} = 1 - \tilde{p}_0 - \tilde{p}_1(\alpha_1 + \alpha_2) - \tilde{p}_2(\alpha_1 + \alpha_2)^2, \qquad (11)$$

where $\alpha_A \equiv |\vec{S}_A/M_A^2|$ is the initial dimensionless spin of hole A, and the fitting parameters are (again, determined by comparison with numerical data):

$$\tilde{p}_0 = 0.04826 \pm 0.00027, \qquad \tilde{p}_1 = 0.01559 \pm 0.00026,$$
$$\tilde{p}_2 = 0.00485 \pm 0.00025. \qquad (12)$$

We note that the uncertainties on the parameters are incomplete, with an undetermined (but presumably negligible) post-Newtonian component.

For the final spin, one model with just enough complexity for our data sets here was given by [64,68][2]:

$$\alpha_{\mathrm{AEI}} = \tilde{\alpha} + s_4 \eta \tilde{\alpha}^2 + s_5 \eta^2 \tilde{\alpha} + t_0 \eta \tilde{\alpha} + 2\sqrt{3}\eta$$
$$+ t_2 \eta^2 + t_3 \eta^3,$$
$$\tilde{\alpha} \equiv \frac{q^2 \alpha_1 + \alpha_2}{q^2 + 1}, \qquad (13)$$

where the coefficients $\{s_4, s_5, t_0, t_2, t_3\}$ were determined by comparison with numerical data:

---

[1]Other models for the post-merger mass are available; see, for instance, Tichy and Marronetti [66] and Lousto et al. [67].
[2]Note that we have adapted Eq. 4 of [68] to match our convention for q.

$$s_4 = -0.1229 \pm 0.0075, \qquad s_5 = 0.4537 \pm 0.1463,$$

$$t_0 = -2.8904 \pm 0.0359, \qquad t_2 = -3.5171 \pm 0.1210,$$

$$t_3 = 2.5763 \pm 0.4833. \qquad (14)$$

In Table IV we present final masses and spins derived from values derived from Eqs. (11) and (13), with uncertainties due only to the parameter uncertainties in Eqs. (12) and (14). Unfortunately since Eq. (11) only applies to equal-mass cases, we cannot use it to estimate the X400 end-state mass. The more complicated formula found in Lousto *et al.* [67] covers more generic binaries, but with larger uncertainties.

We note also from Table IV that the two cases X1DD and X400 have the same final spin, within the quoted uncertainties. Thus we might expect similarities in the ringdown portion of their waveforms across all important modes, though the extent to which each quasinormal mode is excited will be different in the two cases.

B. Multipolar amplitudes

In Ref. [8] we found strong similarity in the peak-scaled modal amplitude development through the peak for a range of nonspinning mergers over a range of masses, and somewhat rougher similarity among the different modes. For nonspinning mergers, the dominant modes were generally those with $\ell = m$, and these modes were neatly described with the IRS heuristic.

Strain-rate amplitudes for the strongest modes of our new simulations are shown in Fig. 1. For all equal-mass simulations, the strongest subdominant modes are (4, 4) and (3, 2); other modes never attain 0.1% of the (2, 2) power [equivalently, 3% of the (2, 2) amplitude]. For X1DD, the (2, 2) mode is even more strongly dominant: in this case, all subdominant modes other than (3, 2) show significant power only at very late times. At $R = 45M$ the (2, 0) mode shows an amplitude similar to the weaker of the modes shown here, but this is sensitive to the extraction radius (our procedure for detrending the strain-rate does not work well for $m = 0$).

It is worthwhile to briefly consider how the modal composition varies with aligned spin and mass ratio, as shown here. Note that the (4, 4) mode amplitude is roughly the same for all cases shown here, varying even less than the (2, 2) amplitudes, as was already seen for the non-spinning runs investigated in [8]. For the equal-mass cases, the (3, 2) mode amplitude roughly equals the (4, 4) mode at peak, but for aligned (antialigned) spins it is enhanced (suppressed) approaching the peak. For the 4:1 mass-ratio X400, the odd $\ell = m$ make significant contributions unseen for equal masses, more so than in the X1UD asymmetric-spin case. For asymmetric mergers of either kind, $\ell = |m| + 1$ modes are also significant.

Figure 2 overlays the (2, 2) (top panel) and (4, 4) (bottom panel) amplitude peaks of all cases (suitably time-shifted and rescaled) to compare their relative sharpness. It is
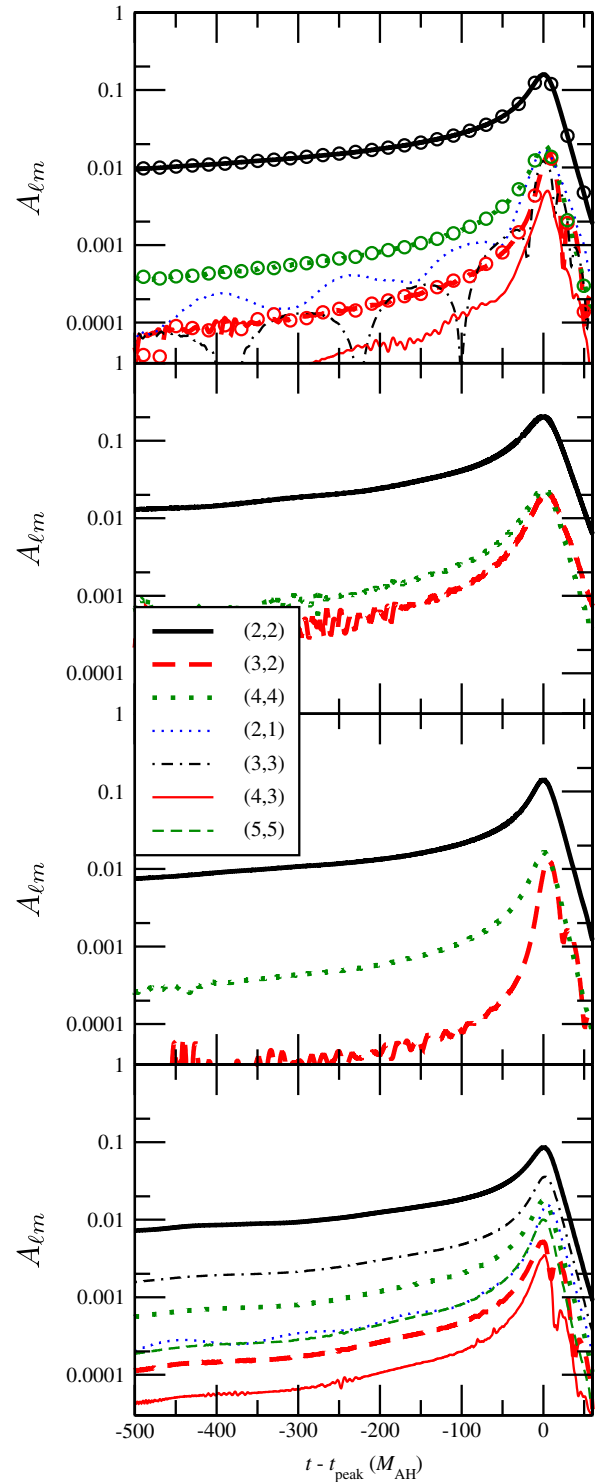

FIG. 1 (color online). Multipolar strain-rate amplitudes for X1UD (top panel), X1UU (second), X1DD (third), and X400 (bottom panel), evaluated at finite extraction radii (45M for the equal-mass, 50M for the X400 case). The lack of symmetry for X1UD and X400 means additional excited (odd-m) modes. For the X1UD case, we overlay circles to show the nearly identical even-m mode amplitudes of X100. In each panel, we omit subdominant amplitudes that never exceed 3% of the (2, 2) mode.
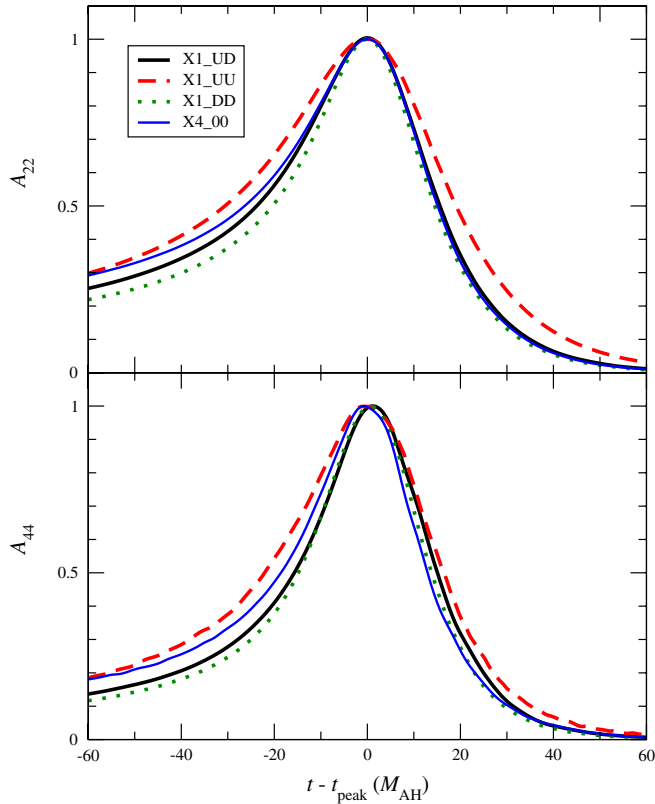
FIG. 2 (color online). Comparison of "sharpness" of amplitude peaks for (2, 2) (top panel) and (4, 4) (bottom panel) modes of all cases. Each amplitude has been rescaled by its maximum value.

interesting that the "down-down" peaks of X1DD are narrower than the "up-up peaks" of X1UU. The steeper slope on the $t > 0$ side can be tied to the generally faster falloff in QNM modes for the prograde modes of the much more slowly rotating black hole generated by the down-down merger. The peaks remain roughly symmetric, with a faster rise as well. This is particularly striking for the subdominant modes.

C. Waveform phasing

In our studies of nonspinning mergers [8], we found strong correspondence in phase development among the different modes, interpreted as near-"corotation" of the implicit-source moments. Specifically, all significant modes displayed a common rotational phase $\Phi_{\ell m}$ up to the time of peak power at merger, deviating by less than 0.025 rad during that time. After the merger, the deviations between modes increased, but for the $\ell = m$ modes this deviation was very slow, $\lesssim 1$ rad over the first $100M$ following merger. For the weaker $\ell \neq m$ modes, the phasing began to differ somewhat earlier and was in some cases less cleanly described by the IRS heuristic.

Modal phase comparisons are more challenging for equal-mass spinning mergers than they were for

nonspinning unequal-mass mergers. As noted above, the symmetries of the configuration and the weakness of radiative spin effects in the inspiral yield only a few significant modes and even these tend to be weak, subject to competition with noise in the simulations, and likely more sensitive to subtleties in the choice of spherical-harmonic basis.

The left panel of Fig. 3 shows the phasing of several strain-rate modes for the up-up case X1UU. Generally, as was the case for nonspinning systems [8], the different (ℓ, m) modes remain approximately in phase up to the merger. As with the nonspinning mergers, the $\ell = m$ cases show the best agreement for $t < 0$. In this case though, because exchange symmetry excludes the odd-m modes, we only have two $\ell = m$ modes to compare up to $\ell = 5$. Two modes present—(4, 2) and (5, 4)—have amplitudes below our 3% cutoff in Fig. 1. Such small amplitudes introduce a lot of noise in the mode's phase; we include the phase only when it begins to show acceptable continuity.

We take a closer look at the relative phasing in the right panel of Fig. 3, where we present the difference between each of the three strongest subdominant modes—(4, 4), (3, 2), and (5, 4)—with the dominant (2, 2) mode. Generally the phase differences decrease going from a finite extraction radius (dashed curves) to $r_{\text{ext}} \rightarrow \infty$ (solid curves).

Looking at the inspiral portion ($t < 0$) of the phase first, we see that the (2, 2) and (4, 4) rotational phases agree within ~ 0.05 rad, with a marginal improvement when we extrapolate $r_{\text{ext}} \rightarrow \infty$. For the (3, 2) mode, there is a roughly constant offset of about 0.15 rad after r_{ext}-extrapolation. Because of the short extent and noisy nature of the reliable (5, 4) mode phase, it is difficult to extract a definite phase offset; it appears to be in the range 0.05–0.10 rad after extrapolation. However, the phase offset has also flipped sign during extrapolation in r_{ext}, indicating that we may not know the correct phase to high accuracy. This may not be resolved simply by increasing grid resolution; we have seen similar extrapolation sign-flips for the (5, 4) phase offset in our X1UD simulations, even at the "ultrahigh" $3M/224$ resolution. As with the nonspinning case, the $\ell \neq m$ modes show the largest offset from the (2, 2) modes, and are most affected by r_{ext}-extrapolation effects.

We note that post-Newtonian theory predicts for nearly constant phase offsets between modes during late inspiral; these come in at 1.5PN order for certain modes (see, for example, the polarization amplitudes given in [69]). However, they are small compared to the phase differences shown here—less than ~ 0.03 rad up to $100M$ before peak.

Looking now at the post-merger period ($t > 0$), the phase agreement remains quite tight, better than that seen in the nonspinning mergers. In the IRS interpretation, all modes in this case remain nearly rotationally locked right
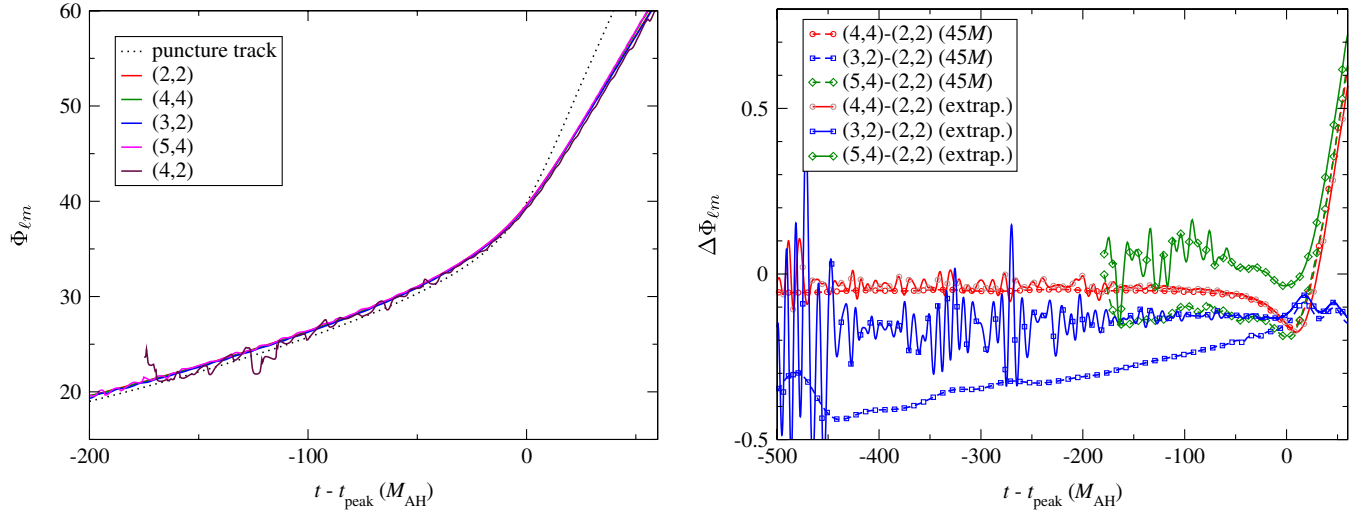
FIG. 3 (color online). Left: rotational phase $\Phi(t)$ from puncture tracks and different multipolar strain-rate components extrapolated to $r_{\rm ext} \to \infty$ for the up-up case X1UU. The weakest two modes, (5, 4) and (4, 2), are only measurable for about $200M$ before merger. Right: the difference in phase with the (2, 2) mode for the next three most important modes only: (4, 4) (circles), (3, 2) (squares), and (5, 4) (diamonds). In each case, we show the difference at $r_{\rm ext} = 45M$ (dashed lines) and $r_{\rm ext} \to \infty$ (solid lines).

through the merger. Note, in particular, that the phase difference between the (2, 2) and (3, 2) modes is roughly constant for $t > 0$. The (4, 4) and (5, 4) modes are also in phase with each other at $r_{\rm ext} = 45M$; they develop a phase offset when extrapolated to $r_{\rm ext} \to \infty$, but maintain the same slope. All modes agree within $\lesssim 1$ rad even $60M$ after peak.

To understand this tight phase agreement, we may look to perturbation theory for the post-merger Kerr hole. For rapidly spinning black holes, QNM frequencies depend primarily on m, approaching $M\omega_{\rm QNM} = m/2$ in the

$a \to M_{\rm f}$ limit [70,71], which suggests a tighter coupling for the modes in this case. However, the final spin of the post-merger Kerr hole for X1UU, $\alpha \approx 0.91$, is not close enough to this extremal limit to explain the phase agreement we see.

In the left panel of Fig. 4 we show the phasing of several modes for the down-down simulation X1DD. Again, the (4, 2) and (5, 4) modes are weak, and yield reliable phases only from $\sim 100M$ before peak. Looking at the right panel, the (4, 4) mode extrapolated phase difference is ~ 0.02 rad, while there is a small offset of about 0.1 rad between the
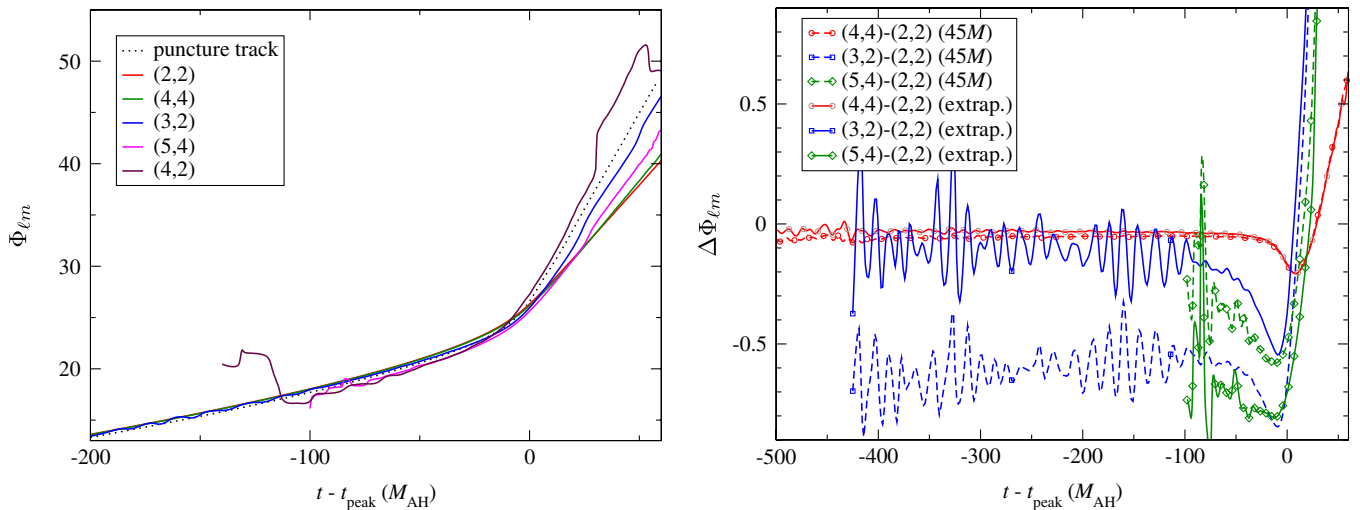

FIG. 4 (color online). Left: rotational phase $\Phi(t)$ from puncture tracks and different multipolar strain-rate components extrapolated to $r_{\rm ext} \to \infty$ for the down-down case X1DD. The weakest two modes, (5, 4) and (4, 2), arise very suddenly at late times, and are only measurable for about $100M$ before merger. Right: the difference in phase with the (2, 2) mode for the next three most important modes only: (4, 4) (circles), (3, 2) (squares), and (5, 4) (diamonds). In each case, we show the difference at $r_{\rm ext} = 45M$ (dashed lines) and $r_{\rm ext} \to \infty$ (solid lines).

(3, 2) and (2, 2) modes. As with the X1UU mode, extrapolation in r_{ext} appears to increase the phase offset. There is a slight drift among the $\ell = m$ modes, similar to that seen in other cases. Indeed, the phase difference between (2, 2) and (4, 4) is nearly identical to that of the X1UU case. The $\ell \neq m$ modes this time show significantly varying frequencies (slopes). This is unsurprising, consistent with the differences among the leading normal QNM mode frequencies.

IV. MODELING THE NEAR-MERGER WAVEFORM

In this section we undertake a more quantitative study of the late-time waveforms through merger and ringdown, following the general approach in [8] for an explicit quantitative representation of the frequency development. We extend the previous work on modeling the amplitude with additional parameters to allow more precise fits at relatively early times.

The waveform phasing examined in the last section is fairly featureless. The phase is monotonic, slowly developing curves with a gentle elbow at merger. This simplicity is a result of the slow secular development of the underlying circular motion which generates the radiation. It also suggests that we may quantify the phase development with just a few parameters.

Following the approach in [8] we probe more deeply into the phasing by taking a time-derivative to study the frequency evolution. Common features are found among the leading waveform modes and across a range of mergers, allowing the results to be summarized with a simple parametrization. With the same general frequency model as in [8] for nonspinning mergers we can also describe the phasing of spinning black-hole mergers.

In Fig. 5, we compare the dominant-mode frequencies of the three equal-mass cases presented above. Since odd-m modes are suppressed by symmetry, the relevant modes are the (2, 2) (quadrupole), (4, 4), and (3, 2) modes. Unsurprisingly, the frequencies are consistently higher throughout merger for more-aligned spins, with the final plateau value matching the dominant QNM frequency. For the (3, 2) modes, there is significant deviation from the smooth frequency development generally expected according to our IRS heuristic; this amounts to a large bump in the frequency during the plateau phase. Similar deviations in the (3, 2) modes have been noted previously [8,72]. Such effects may arise through mode mixing with the (2, 2) mode [73], which could arise through ambiguity in the shape of the sphere on which the radiation is measured, or on the use of (spin-weighted) spherical harmonics, rather than the spheroidal harmonics appropriate for the perturbation theory in which the QNM frequencies are defined [74]. The precise cause and mechanisms of this mixing are open questions, which we hope to return to in future work.
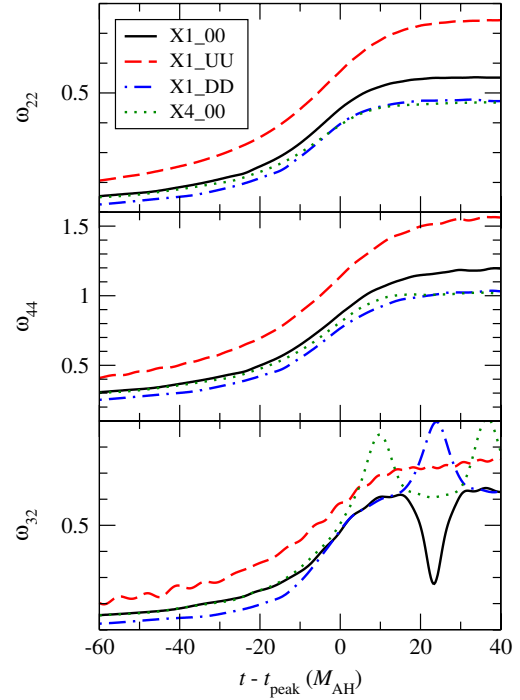

FIG. 5 (color online).   Waveform frequency $\omega_{\ell m}$ for the dominant modes of the equal-mass evolutions. The upper panel shows the dominant (2, 2) mode, while the middle and bottom panels show the next strongest modes—(4, 4) and (3, 2), respectively. We also show the corresponding frequencies for the 4:1 non-spinning merger X400. At early times, this tracks the X100 waveform, while during merger it approaches the final frequency of the X1DD case.

Also included in Fig. 5 are the equivalent frequencies for the 4:1 nonspinning merger X400 (note, however, that that merger had significant odd-m modes not present in the equal-mass cases here). The spins of the antialigned X1DD initial data were chosen to yield the same final Kerr parameters (mass, spin) as the X400 data, according to (13). As the Kerr parameters determine the QNM frequencies of each mode, it is not surprising that the X1DD and X400 frequencies level off to the same value after merger. What is interesting is the difference in behavior approaching this final state. For $t \lesssim -20M$, X400 hews closely to the nonspinning X100. The latter could be expected given the similarity in phasing upon approach to merger for nonspinning mergers [8]. At the latest times the frequency development is determined primarily by the parameters of the final black hole formed, while additional parameters become important as we look back to earlier times.

A. Modeling the rotational frequency

In [8], we introduced the following empirical model for the rotational frequency $\Omega_{\ell m} \equiv \omega_{\ell m}/m$ in a short time window around the merger:
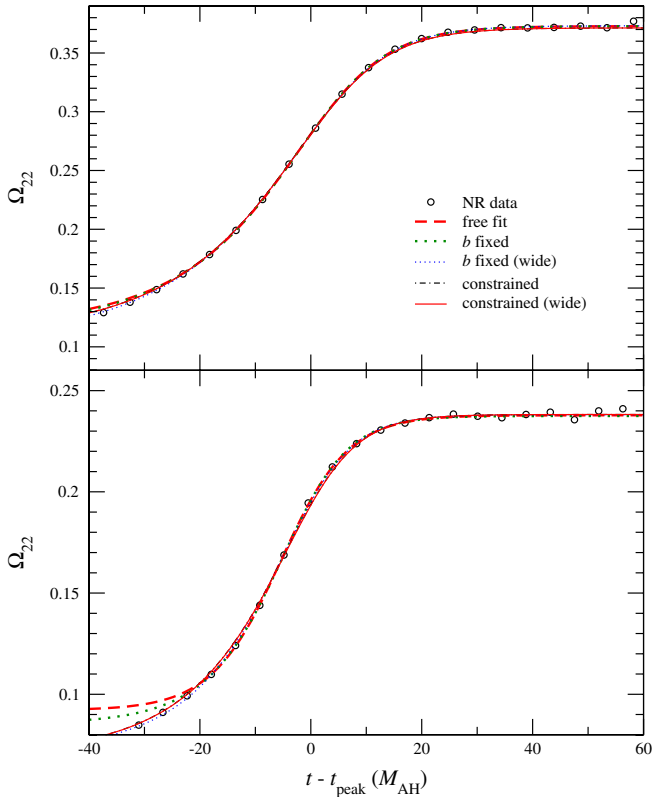
FIG. 6 (color online).   Rotational frequency fits for the (2, 2) modes of the X1UU (top) and X1DD (bottom) runs, extrapolated to $r_{ext} \to \infty$. The different fits differ primarily in the early part of the comparison window around t_{peak}, which runs from $-20M_{AH}$ to $+40M_{AH}$ for standard fits, and from $-40M_{AH}$ to $+60M_{AH}$ for wide fits.

$$\Omega(t) = \Omega_f(1 - \hat{f}(t)) \qquad (15)$$

$$\hat{f}(\kappa, b, t_0; t) = \frac{c}{2}\left(1 + \frac{1}{\kappa}\right)^{(1+\kappa)}\left[1 - \left(1 + \frac{1}{\kappa}e^{-2(t-t_0)/b}\right)^{-\kappa}\right], \qquad (16)$$

where the dimensionless parameter $c = \dot{\Omega}_0 b/\Omega_f$ replaces the "maximum frequency slope" $\dot{\Omega}_0$ corresponding to the peak chirp rate. Within this general framework, there are

up to five free parameters for the frequency development: c, κ, b, t_0, and Ω_f.

In our previous investigations [8], this functional form worked well in fitting the dominant frequencies of a sequence of nonspinning binaries with mass ratios in the range $\{1.0, 6.0\}$. Unsurprisingly, Ω_f was found to be consistent with the quasinormal frequency of the post-merger Kerr hole. More interestingly, b was also found to be approximately consistent with the quasinormal damping time, meaning that at late times the frequency approaches its limiting value exponentially at the same rate as amplitude squared. It was also found that the dimensionless ratio $M_f\dot{\Omega}_0/\Omega_f \approx 0.021$ across all cases.

We usually apply (15) as an "orbital frequency", which is scaled from the gravitational-wave frequency by the azimuthal mode number m. The formula may be applied, with similar results, to strain, strain-rate, or ψ_4 waveforms.

We consider three increasingly constrained classes of fits of this form. The most general is a free fit for all five parameters. Second, we test the late-time frequency/amplitude relationship noted in [8] with a fit where b is constrained to agree with the late-time amplitude falloff rate (and thus with the QNM falloff rate). Finally we suggest a general fit by which all parameters (other than t_0) are derived from the final black-hole mass and spin.

We focus on the strain-rate fit, as it provides a good compromise between the baseline drift error that affects the strain waveforms, and the higher level of noise in the ψ_4 waveforms. Figure 6 shows the result of this procedure for the r_{ext}-extrapolated waveforms of the X1UU (top) and X1DD (bottom) runs (note that the numerical data have been down-sampled by factors of 20 or more for clarity of presentation). At the level of precision accessible by eye all fits appear nearly perfect after $t > -20$. Parameter fits conducted only over times $t > -20$ typically do not extrapolate well to earlier times; a fit over a wider range, extending over $t > -40$ appears to be very good over this entire region though there is some slight degradation in the quality of the fit near $0 < t < 10$. For the dashed curves labeled "free fit," all five parameters in (16) were fit freely against the numerical data. In the curves labeled "b fixed," we test the hypothesis that the exponential decay of

TABLE V.   Best-fit values for the unconstrained parameters c, κ, b, Ω_f, and t_0 for the frequency model (15), and of A_0 and α_1 for the amplitude model (17). All fits are over a time window from $t_{peak} - 40M$ to $t_{peak} + 60M$. Quoted uncertainties are the direct sum of three terms: uncertainties in the highest-resolution fits; differences between best-fit values for $r_{ext} \to \infty$ and $r_{ext} = 45M$ (40M for X400); and differences between best-fit values at highest and next-highest resolutions runs.

Run name	c	κ	t_0	b	Ω_f	A_0	α_1
X100	0.2489 ± 0.0040	0.421 ± 0.015	-3.77 ± 0.17	11.685 ± 0.025	0.27655 ± 0.00021	1.270 ± 0.022	6.64 ± 0.35
X1UU	0.2500 ± 0.0021	0.401 ± 0.009	-2.15 ± 0.59	14.296 ± 0.030	0.37317 ± 0.00070	1.627 ± 0.064	2.46 ± 0.70
X1DD	0.2626 ± 0.0062	0.473 ± 0.027	-4.90 ± 0.12	11.203 ± 0.034	0.23805 ± 0.00093	1.157 ± 0.009	11.12 ± 0.12
X1UD	0.2458 ± 0.0038	0.407 ± 0.014	-3.57 ± 0.15	11.634 ± 0.024	0.27643 ± 0.00017	1.263 ± 0.016	6.27 ± 0.38
X400	0.2343 ± 0.0033	0.439 ± 0.009	-4.73 ± 0.52	11.381 ± 0.033	0.23380 ± 0.00075	0.740 ± 0.017	9.96 ± 1.26

frequency evolution is related to the amplitude falloff rate, fixing b first by a fit to the exponential decay rate in the mode amplitude data, before fitting the other parameters according to the frequency data. Though the frequency data are then fit against four parameters instead of five, the result is still a very good fit, justifying the assumption. The amplitude/frequency relationship is discussed more in the next section. With b based on the amplitude data, we record the best-fit values of the parameters c, κ, b, Ω_f, and t_0 in Table V. The final curves in Fig. 6 (labeled "constrained") only fit t_0, with all other parameters preset, as discussed below in Sec. IV C.

B. Amplitude modeling

Following [8], our strategy is to describe the wave amplitudes in relation to the frequency. This is loosely motivated by the idea that frequency evolves in response to loss of energy and angular momentum, but energy and angular momentum fluxes are dependent on the wave amplitude. For nonspinning systems, we previously found that $dJ/d\Omega$ was slowly varying in the merger, and could be approximated as a constant. The result was enough to provide a coarse quantitative description of the merger-ringdown amplitude development in reference to the frequency development. Here we extend that model, introducing additional parameters to allow more precise quantitative description of the numerical results.

Now assume the waveform strain-rate amplitude takes the general form:

$$A_{\ell m}(\hat{f}) = A_{0\ell m} P(\hat{f}) \sqrt{|\dot{\hat{f}}(t)|}, \qquad (17)$$

where the adjusting function $P(x)$ is some function that approaches unity as $x \to 0$. Then assuming that the strain amplitude $H_{\ell m}$ satisfies $|\dot{H}_{\ell m}| \ll |H_{\ell m} \dot{\varphi}_{\ell m}^h|$, which is true at all points of the numerical waveform, we can find an approximate expression linking strain and strain-rate:

$$A_{\ell m} \approx H_{\ell m} \omega_{\ell m}^h. \qquad (18)$$

Combining this with (17), we can model the *strain* amplitude as:

$$
\begin{aligned}
H_{\ell m}(\hat{f}) &= \omega_{\ell m}^{-1} A_{\ell m}(\hat{f}) \\
&= (m\Omega_f)^{-1}(1 - \hat{f})^{-1} A_{0\ell m} P(\hat{f}) \sqrt{|\dot{\hat{f}}(t)|} \\
&= H_{0\ell m}(1 - \hat{f})^{-1} P(\hat{f}) \sqrt{|\dot{\hat{f}}(t)|}.
\end{aligned}
\qquad (19)
$$

Similarly, the amplitude of the ψ_4 (ℓ, m) mode would be modeled as:

$$C_{\ell m}(\hat{f}) = C_{0\ell m}(1 - \hat{f}) P(\hat{f}) \sqrt{|\dot{\hat{f}}(t)|}, \qquad (20)$$

where we are still using the strain sign convention for phasing of modes (that is, positive-m modes have positive frequencies).

Parameters including A_0 and other parameters in the definition of $P(\hat{f})$ allow some tuning for various cases considered here while preserving the general approach in [8]. Concretely, consider

$$P(\hat{f})^{-2} = 1 + \sum_{n=1}^{N} \alpha_n (\hat{f}^{2n} - \hat{f}^{2n+2}). \qquad (21)$$

The simplest possibility, with $N = 0$ yielding $P = 1$, would imply that $dE/d\omega$ is constant, i.e. that the system loses radiative energy in linear proportion to the late-time frequency decay to the quasinormal-ringdown rate; this is close to the amplitude model used in [8]. Equation (21) is consistent with quasinormal ringing radiation in the $f \to 0$ limit (assuming frequency model parameter $b = 1/\Im\omega_{QNM}$) and can be adjusted for deviations earlier in the waveform where $1 > f > 0$. The restriction to even powers was motivated by an empirical observation that the first helpful correction seems to be at second order, and the resummed powers in the summand, yields a more generally regular result as $f \to 1$. Going back to
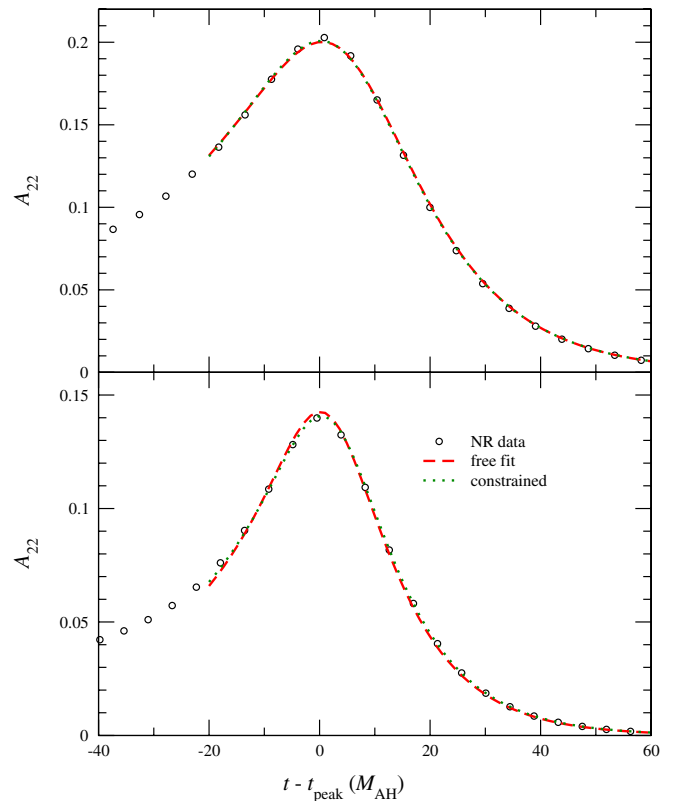

FIG. 7 (color online). Amplitude fits for the (2, 2) modes (extrapolated to $r_{ext} \to \infty$) of the X1UU (top) and X1DD (bottom) runs. The two fits in each panel differ in whether they fit the parameter α_1 or just A_0. The fit windows here emphasize the late tail of the amplitude, running from $-20M_{AH}$ to $+120M_{AH}$.

times more than $20M$ before merger the model becomes unrealistic. The model amplitude begins small at early times, growing exponentially toward the peak.

In practice, we find that we get a good approximation for the merger-ringdown part of the radiation in the (2, 2) modes by keeping one term in the expansion (21), and fitting for A_0 and α_1. Then using $\hat{f}$ from (16), the complete amplitude model used is:

$$A_{22}^2 \equiv |r\dot{h}_{22}(\hat{f})|^2 = A_0^2 \frac{\dot{\hat{f}}(t)}{1 + \alpha_1(\hat{f}^2 - \hat{f}^4)}. \qquad (22)$$

The result of this procedure is shown in Fig. 7, for the r_{ext}-extrapolated waveforms of the X1UU and X1DD runs. For the less-constrained fits, b was first determined using data in a window from $20M_{\text{AH}}$ to $80M_{\text{AH}}$; this value was then fixed, and data over the larger window $-20M_{\text{AH}}$ to $110M_{\text{AH}}$ were used to determine A_0 and α_1. Though not shown in the figure, we see somewhat less accurate fits with the model for the amplitudes of the X400 case, with differences before and near peak at the $\sim 5\%$ level.

C. Constraining the models

Working with the results of the free fits for frequency and amplitude, we note the approximate constancy of the parameters c and κ across all cases. Additionally, we note that the final frequency and decay parameters Ω_{f} and b are close to the expected QNM values. Thus we may be able to reduce considerably the number of free parameters needed for the models.

Similar to the dimensionless scaling used for the c parameter above we seek a scaling of α_1 in terms of the QNM "quality factor" $Q = \Re\omega_{\text{QNM}}/2\Im\omega_{\text{QNM}}$, as a simple dimensionless number dependent on the spin of the final hole. We find that the results for our equal-mass cases roughly scale with Q^2, with the mean result $\alpha_1 \sim 72.3/Q^2$.

We now perform a more constrained version of the fits, fixing the parameters b, Ω_{f} to their QNM values, and replacing c and κ with their average values from Table V,

and setting the frequency parameters and α_1 as outlined above. The combined set of constrained parameters is:

$$c = 0.252, \qquad \kappa = 0.426, \qquad \Omega_{\text{f}} = \Re\omega_{\text{QNM}}/2,$$
$$b = 1.0/\Im\omega_{\text{QNM}}, \qquad \alpha_1 = 72.3/Q^2. \qquad (23)$$

Thus we are left with just two free parameters to fit: t_0 and A_0. These (as well as the constrained parameters) are recorded in Table VI.

We may consider attempting to constrain the remaining parameters as well. The A_0 parameter has units $M_{\text{f}}^{1/2}$ and seems to scale approximately with $\Omega_{\text{f}}^{-1/2}$. Using the mean fit for the equal-mass cases we get:

$$A_0 \sim 9.9\eta\Omega_{\text{f}}^{1/2}. \qquad (24)$$

We include η in the fit since the overall amplitude coefficient must vanish linearly as the mass-ratio goes to zero. Though we have not focused on mass-ratio dependence, this scaling is consistent with the nonspinning 4:1 result.

D. Subdominant modes

As noted above the most significant modes for equal-mass mergers are the (4, 4) and (3, 2) modes. Even these have amplitudes of no more than about one-tenth that of the (2, 2) mode. While the (3, 2) mode shows more complicated features that do not lend themselves to this fitting analysis, the (4, 4) mode is phenomenologically similar to the (2, 2) mode. Figure 8 shows the frequency and amplitude fits for the (4, 4) mode of the X1DD run. The frequency fit is clearly still very close to the numerical data over the domain of interest, but the amplitude's overall peak is $\sim 10\%$ too low, with a poor fit to the slope of the numerical data before the peak. This suggests that our ansatz for the mode amplitude does not carry over to subdominant modes, and requires further work. Nevertheless, we will see in the next section that the dominant mode may already be useful in detection studies.

To contrast the quality of the fit performance for the (2, 2) and (4, 4) modes, we present in Fig. 9 the associated

TABLE VI. Values for the parameters c, κ, b, Ω_{f}, and t_0 for the frequency model (15), and of A_0 and α_1 for the amplitude model (17). Unlike in Table V, only t_0 and A_0 are freely fit; the remaining parameters have been fixed, as given in Eq. (23). All fits are over a time window from $t_{\text{peak}} - 40M$ to $t_{\text{peak}} + 60M$. Quoted uncertainties are the direct sum of three terms: uncertainties in the highest-resolution fits; differences between best-fit values for $r_{\text{ext}} \to \infty$ and $r_{\text{ext}} = 45M$ (40M for X400); and differences between best-fit values at highest and next-highest resolutions runs.

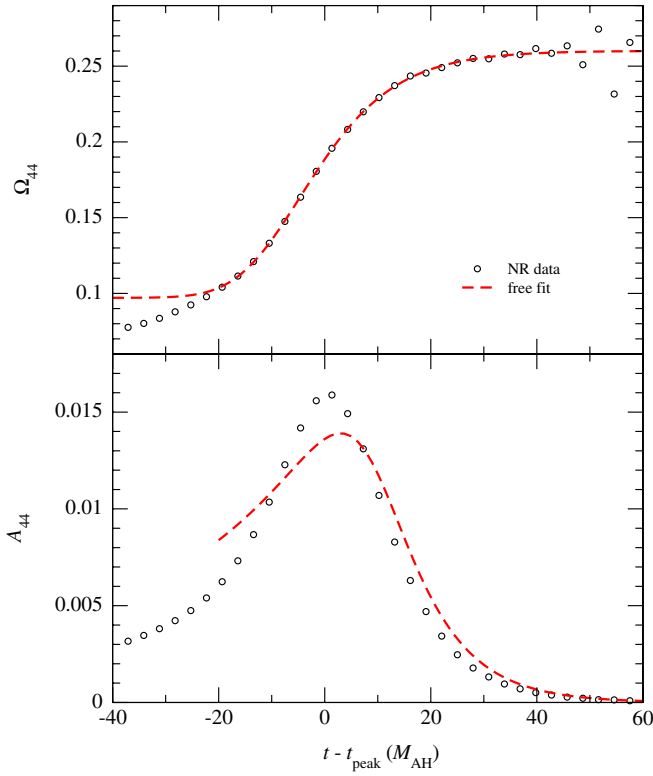| Run name	c	κ	t_0	b	Ω_{f}	A_0	α_1
X100	0.252	0.426	-3.99 ± 0.29	11.712	0.27661	1.271 ± 0.013	6.7934
X1UU	0.252	0.426	-2.31 ± 0.58	14.404	0.37133	1.633 ± 0.032	2.4924
X1DD	0.252	0.426	-4.41 ± 0.36	11.222	0.23820	1.143 ± 0.006	9.9784
X1UD	0.252	0.426	-3.91 ± 0.30	11.681	0.27661	1.272 ± 0.006	6.8296
X400	0.252	0.426	-6.67 ± 0.72	11.465	0.23305	0.732 ± 0.009	9.9867

FIG. 8 (color online). Frequency (top panel) and amplitude (bottom panel) fits for the (4, 4) mode (extrapolated to $r_{ext} \rightarrow \infty$) of the X1DD run. Again, the numerical data are indicated by circles, with a free fit over the parameters represented by the dashed line.

FIG. 9 (color online). Real part of the (2, 2) (top panel) and (4, 4) (bottom panel) strain-rate modes for the X1DD run (extrapolated to $r_{ext} \rightarrow \infty$). Again, the numerical data are indicated by circles, with a free fit over the parameters represented by the dashed line. For the (2, 2) mode, we also include the result of the fully restricted waveform [see Eqs. (23)] as a continuous line.

strain-rate (real parts) over the range of the fit. We also plot in the upper panel the (2, 2) mode resulting from a fully constrained model for amplitude and phase, using Eqs. (23) and (24).

V. FAITHFULNESS OF THE FREQUENCY MODEL

One way to quantify how much of the merger information we have captured by the modeling above is to compare the results of the model with the original fully numerical waveforms in a detector context. We consider an explicit waveform model restricted to the (2, ±2) modes, which contain most of the power. The waveform phase is derived from integrating the model IRS frequency given by (15) and (16), while the amplitude is given by (22).

In total there are seven parameters in these expressions, and one additional parameter φ_0 arises as an integration constant in deriving the phase from our frequency model. Drawing on the results of Sec. IV C, five of these parameters $\{c, \kappa, b, \Omega_f, \alpha_1\}$ are specified by (23) as functions of the final black hole's leading quasinormal-mode frequency, thus reducing these free parameters to functions of the final black hole's mass and spin. Beyond these the only remaining parameters are $\{\varphi_0, t_0, A_0\}$, corresponding to phase and time references, and an overall amplitude scale. For the
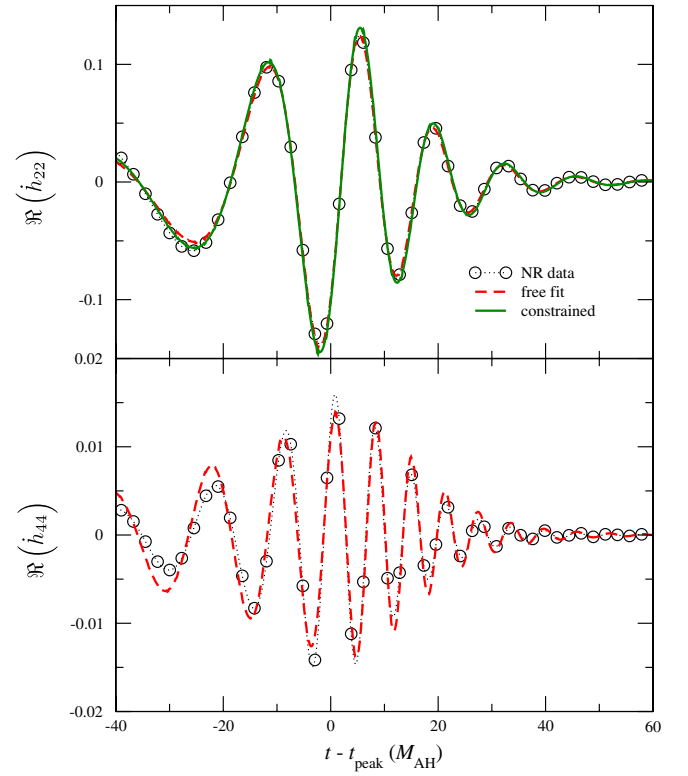
X1DD data, we can see the resulting waveform in the top panel of Fig. 9. For comparison we also show the results of a "free" fit, where the frequency was fit to the NR data without the constraints in (23), and the amplitude was fit based on those results without constraint on α_1. This is not a completely free fit, since the frequency parameters are fit without regard for the consequences on the amplitude.

We calculate the mismatch for the Advanced LIGO detector [75]. "Mismatch" here is defined as the deviation of the normalized overlap integral from unity, usually optimized over free parameters such as overall phase and arrival time [76]:

$$\text{mismatch} \equiv 1 - \max_{\lambda_i} \frac{\langle h_m(\lambda_i)|h_e \rangle}{\sqrt{\langle h_m(\lambda_i)|h_m(\lambda_i)\rangle\langle h_e|h_e\rangle}}, \quad (25)$$

where the frequency-space inner product $\langle \cdot | \cdot \rangle$ is the *overlap* between two signals, defined as [77]

$$\langle h_1|h_2 \rangle \equiv 2 \int_0^\infty \frac{[\tilde{h}_1(f)\tilde{h}_2(f)^* + \tilde{h}_1(f)^*\tilde{h}_2(f)]}{S_n(f)} df$$

$$= 4 \,\text{Re}\left[\int_0^\infty \frac{\tilde{h}_1(f)\tilde{h}_2(f)^*}{S_n(f)} df\right], \quad (26)$$

where $\tilde{h}_1(f)$ and $\tilde{h}_2(f)$ are the Fourier transforms of the signals, and $S_n(f)$ is the (one-sided) noise power spectral density of the detector we are interested in; in this case, we take the ideal form $S_n(f)$ for Advanced LIGO given in Appendix A of [14]:

$$
S_n(f) = S_0 \Big\{ x^{-4.14} - 5x^{-2} \\
+ 111 \Big(1 - x^2 + \frac{x^4}{2} \Big) \Big(1 + \frac{x^2}{2} \Big)^{-1} \Big\}, \quad (27)
$$

where $x \equiv f/f_0$, $S_0 = 10^{-49}$ and $f_0 = 215$ Hz.

For this test, we pick black-hole binaries of total mass $M \in \{40 M_\odot, 300 M_\odot\}$, at a fixed distance of 1 Gpc from the detector. Furthermore, we assume the system is observed along the polar axis. The resulting mismatch with the quadrupole NR signal is shown for all the runs (X100, X1UU, X1DD, and X400) in Fig. 10. Common to all cases is a sharp falloff (that is, improvement) in mismatch as the system mass increases: from $\gtrsim 25\%$ at $M = 40 M_\odot$ to $\lesssim 1\%$ for $M > 200 M_\odot$. This trend is expected: overall physical frequencies scale inversely with system mass, so while the last few premerger orbits' worth of radiation for a $40 M_\odot$ system might fall in Advanced LIGO's most sensitive frequency band, only the higher-frequency merger and ringdown might lie in the same band for a $200 M_\odot$ system.

In Fig. 11 we again show this mismatch for the X100 configuration, along with three other mismatches: with the *full* NR signal (all modes) along the polar axis, and on the equatorial plane, and also against the *unconstrained* model, using "free"-fit parameters (Table V). This last mismatch has been scaled up by a factor of 100 for visibility.
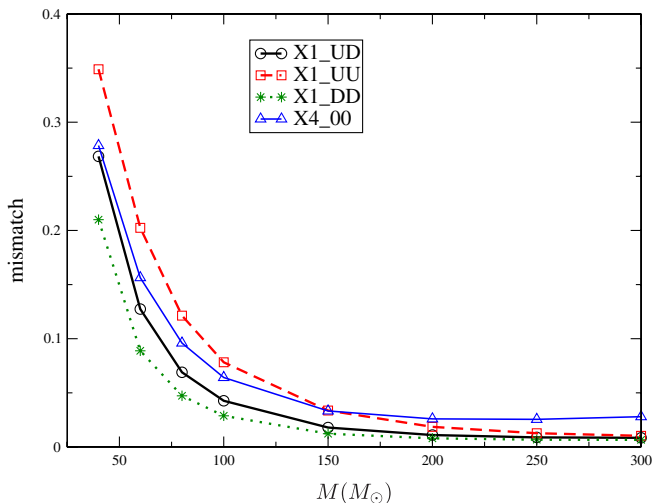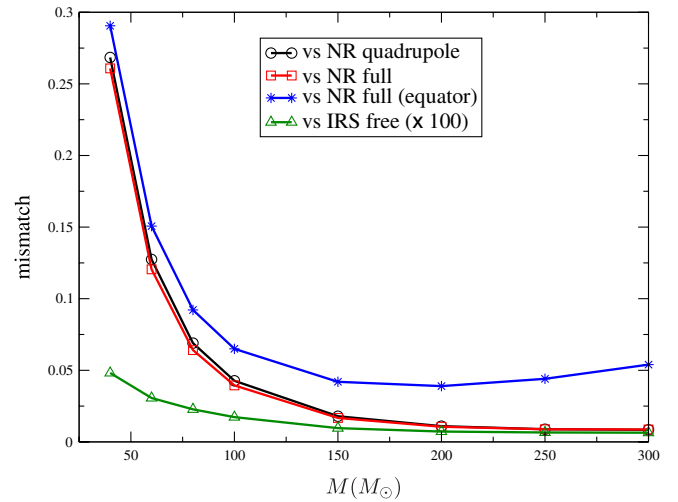

FIG. 11 (color online). Mismatch (25) for the X100 configuration, between quadrupole $(2, \pm 2)$ constrained IRS waveforms and (1) quadrupole numerical-relativity waveforms along the polar axis (circles), (2) full NR waveforms along the polar axis (squares), (3) full NR waveforms on the equator (stars), and (4) the unconstrained IRS waveforms along the polar axis (triangles). All mismatches were calculated in the context of the Advanced LIGO detector, at a distance of 1 Gpc.

For these results we have compared with just the (2, 2) component of our numerical simulation waveforms. If applied in an actual observation there would be additional power, perhaps at the level of up to several percent in other harmonics. This model makes no attempt to fit those contributions. With a little work we could extend our constrained model to approximate the contributions of these other modes, but this would necessarily require dependence on many additional parameters, including information about the component masses and spins and the relative orientation of source and detector.

We note that the the "sweet spot" of the Advanced LIGO sensitivity curve (27) is around 200 Hz. For systems at the low-mass end of our plot, $40 M_\odot$, this frequency range is accurately handled by post-Newtonian-based waveforms. Thus a full waveform model appropriate for such low-mass systems should really be a combination of our merger-ringdown model with a PN-based inspiral. By neglecting this here, and integrating over the full band, we will suffer from junk numerical radiation and windowing artifacts at the lower-mass end. It is reasonable to suspect that we would get a considerably lower mismatch if we restricted our integration to frequencies above $M \omega_{22} \approx 0.15$. The estimates presented in Figs. 10 and 11 are therefore likely to be conservative.

With one detector, signals based on the waveform model we have constructed here depend only on the intrinsic parameters describing the final black hole, phase and time references and overall amplitude, just five of the 17 parameters describing generic black-hole merger observations. Our results suggest that dominant features of the

FIG. 10 (color online). Mismatch (25) between quadrupole $(2, \pm 2)$ constrained IRS and numerical-relativity waveforms for all simulations in the context of the Advanced LIGO detector, where the system was observed along the polar axis at a distance of 1 Gpc.

powerful merger-ringdown radiation may be described with little or no reference to the details of the component black holes. This provides a complementary description of the merger to those based on the binary inspiral parameters. Even without a long inspiral lead-in, such models may be useful in detecting gravitational waves from high-mass mergers. Our waveforms are based on the same parameters as those in ringdown-based approaches to merger observations in ground-based detector pipelines [78–81] and may be useful in future versions of these searches.

VI. DISCUSSION

In this paper, we have investigated the mode-decomposed gravitational waveforms resulting from the merger of aligned-spin black-hole binaries. Our primary purpose was to establish how well the implicit rotating source picture of the binary as a GW source—first suggested in [8] in the context of nonspinning holes of comparable mass—holds in this different branch of parameter space.

Based on these investigations, we note that the modal structure of aligned-spin mergers is like that of the equal-mass nonspinning configuration, dominated by the $(2, \pm 2)$, $(3, \pm 2)$, and $(4, \pm 4)$ modes. These modes still display IRS-type behavior, featuring common rotational phase evolution with little offset through late-inspiral, merger, and into ringdown. The peak modal amplitudes are similar to those for the nonspinning case, though the duration of the peak region (which was roughly independent of mass ratio) is extended for aligned spins (and shortened for antialigned spins). A similar time-scale dependence is seen in the rise to peak frequency.

In applying our late-merger frequency model (with a slightly modified parametrization) to these new cases, we have found that the model still performs well for the dominant modes. We enhance the original mode amplitude model of [8] to achieve improved behavior, at least for the leading $(2, \pm 2)$ modes; however it yields up to $\sim 10\%$ mismatches at and before peak for the next most important modes.

For the $(2, \pm 2)$ modes at least, we have attempted to constrain all parameters explicitly with reference only to the state of the final black hole (i.e., its dominant quasinormal-mode complex frequency). With these constraints, we have reduced the additional free parameters to just three: t_0, the time of maximum chirp-rate; φ_0, the phase offset; and A_0, the mode's amplitude scale. This description provides an approximate fit to the late part of the waveforms for all our simulations, including equal-mass spinning cases, and the 4:1 nonspinning case. Moving back in time to earlier points before the merger, the quality of this fit degrades and other physical details of the premerger binary become more significant. We see evidence of this when comparing the X400 (4:1

nonspinning) and the X1DD (equal-mass down-down spins) configurations, which result in the same final spin.

We have quantified the quality of this approximation by calculating Advanced LIGO fitting factors. For system masses of $\gtrsim 150 M_\odot$, we have found mismatches of $\lesssim 5\%$ between the full numerical-relativity waveform and the $(2, \pm 2)$-mode-only model waveforms.

Our results suggest that an approach to gravitational-wave observation templates with parameters tied first to the structure of the final black hole may be useful for Advanced LIGO observations of intermediate-mass mergers. These would be an alternative to the time-domain effective-one-body templates of [82–84], and the frequency-domain ''phenomenological'' templates of [18,19], similar to ringdown searches currently being applied to LIGO data [78–81]. In future work we plan to investigate the quality of this model, or its extensions, for a broader variety of mergers, including precessing and eccentric configurations.

In this explicit modeling, we have focused on the dominant (2, 2) mode. A similar model incorporating full multimode information can also be applied to complete inspiral-merger-ringdown waveform templates, as was done for nonspinning systems in [8]. Future work on this topic will focus on improving and extending the amplitude model to cover multiple significant modes of the merging binary.

APPENDIX: CONVERGENCE

In this appendix, we present the convergence properties of the evolution fields and extracted waveforms. Our presentation will model that of [8].

The simulations X100, X1DD, and X1UD used identical numerical methods and grid structures, with finest (near-puncture) resolutions of $3M/128$, $3M/160$, and $M/64$, and wave-extraction-region resolutions of $3M/2$, $6M/5$, and M, respectively. The X1UD simulation was also carried out at an ultra-high resolution of $3M/224$ (wave-extraction resolution $6M/7$).

The remaining equal-mass simulation, X1UU, uses identical numerical methods at the same resolutions, but had a different grid structure in the wave-extraction zone. This has been seen to result in higher noise levels in waveform quantities, but should not affect the overall convergence properties. We will use the X1UD resolution to assess convergence levels for the HAHNDOL/PARAMESH code.

1. Constraints

To establish constraint convergence in the equal-mass runs, we look at the L1-norms of the Hamiltonian and momentum constraints both in the strong-field region and in the region where the waveforms are extracted.

Figure 12 shows the L1-norm of the Hamiltonian constraint. In the upper panel, level 13 (the region just outside the punctures) demonstrates between fourth- and fifth-order convergence; in the lower panel, level 8 (containing the wave-extraction spheres) demonstrates diminished convergence—between second and third order. Note that the resolution in these outer regions is much lower than in the crucial high-resolution regions, where the black holes reside. It is our understanding that errors in these distant regions are dominated by the effects of uninteresting short-wavelength features (particularly gauge modes), which propagate out from the center and become poorly resolved in the coarse regions.

Convergence is more difficult to establish for the momentum constraint. Figure 13 shows the behavior of the x component's L1-norm in level 14 (the region containing the punctures), and level 8 (containing the wave-extraction spheres). The very inner zone (level 14)—displays clean behavior: all components of the momentum constraint are

FIG. 13 (color online). Convergence of the momentum constraint's L1-norm for the X1UD simulation: between second- and third-order convergence in level 14 (upper panel); without any established convergence order in level 8 (lower panel).
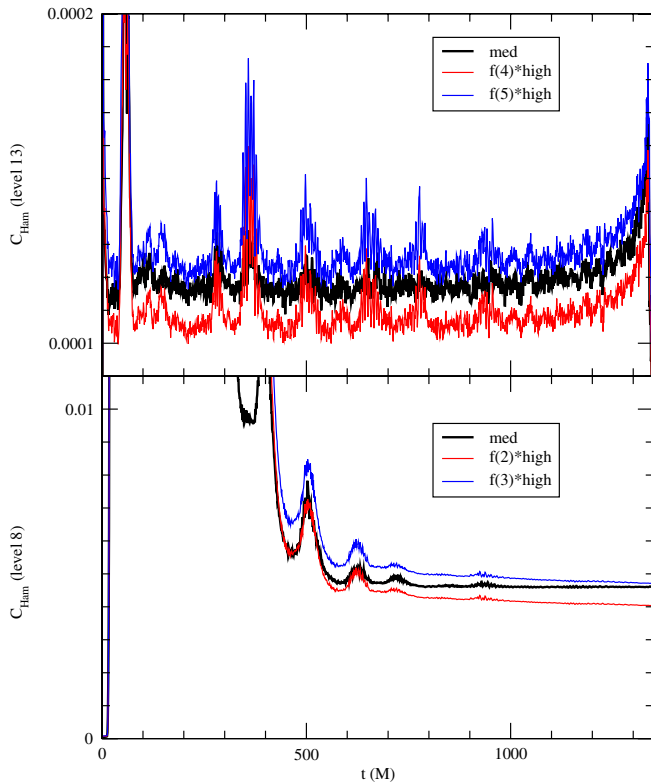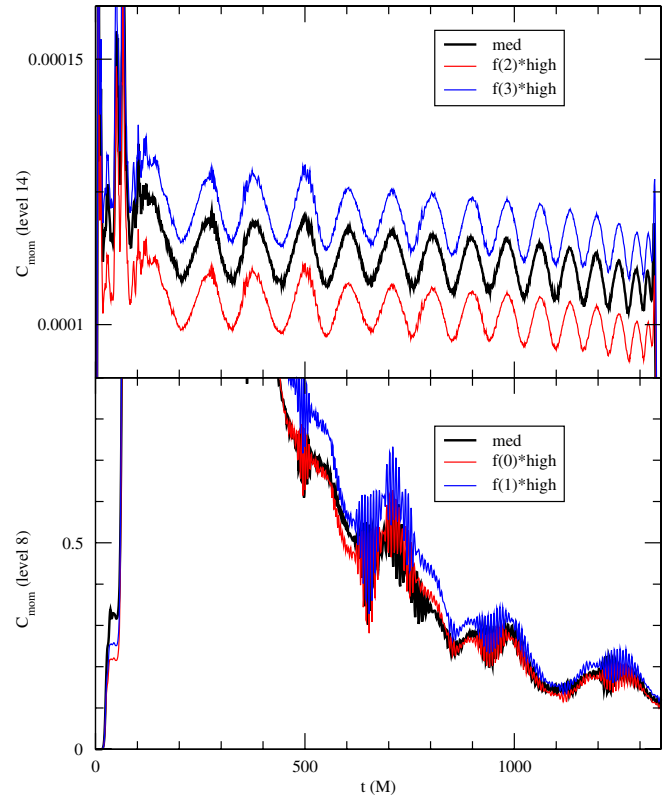

FIG. 12 (color online). Convergence of the Hamiltonian constraint's L1-norm for the X1UD simulation: between fourth- and fifth-order convergence in level 13 (upper panel); between second- and third-order convergence in level 8 (lower panel).
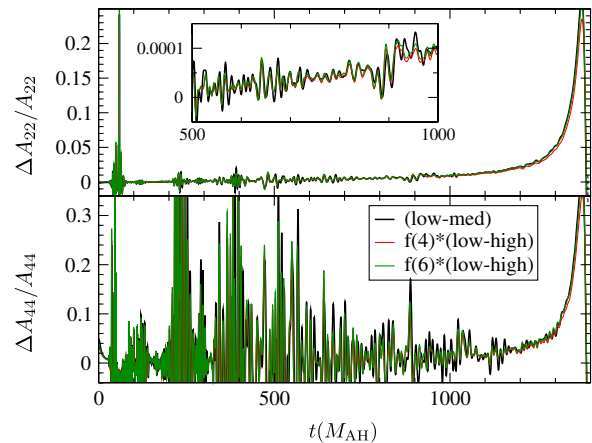

FIG. 14 (color online). Amplitude convergence for the (2, 2) (upper panel) and (4, 4) (lower panel) modes of the X1UD simulations, based on the central resolutions $3M/160$, $M/64$, and $3M/224$. In each case, the $(3M/160 - 3M/224)$ difference has been scaled up assuming fourth- and sixth-order convergence. Though noisy, the amplitude differences appear to be consistent with sixth-order convergence throughout the inspiral, until $\sim 150M$ before merger.
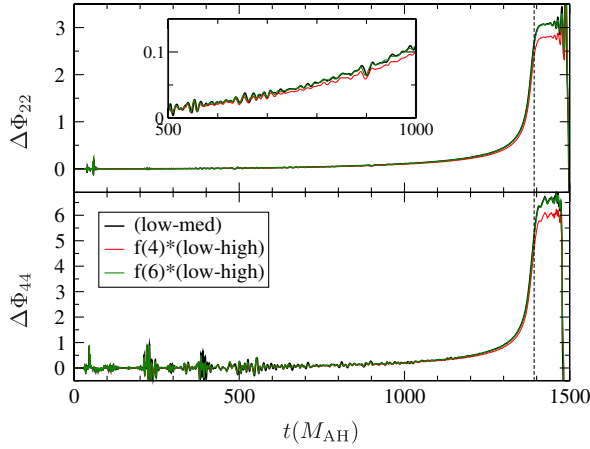
FIG. 15 (color online). Phase convergence for the (2, 2) (upper panel) and (4, 4) (lower panel) modes of the X1UD simulations, based on the central resolutions $3M/160$, $M/64$, and $3M/224$. In each case, the $(M/64 - 3M/224)$ difference has been scaled up assuming fourth- and sixth-order convergence. The phase differences appear to be consistent with sixth-order convergence throughout the inspiral, merger, and ringdown.
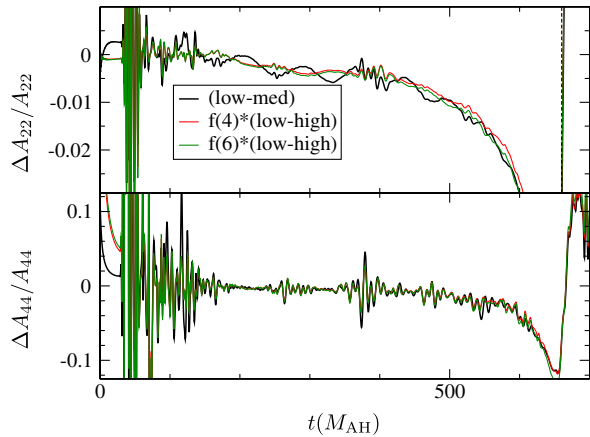

FIG. 16 (color online). Amplitude convergence for the (2, 2) (upper panel) and (4, 4) (lower panel) modes of the X400 simulations, based on the central resolutions $M/96$, $M/128$, and $M/160$. In each case, the $(M/96 - M/160)$ difference has been scaled up assuming fourth- and sixth-order convergence. The amplitude differences appear consistent with sixth-order convergence until approximately $60M$ before peak, when the rate declines to close to fourth order.

roughly 2.6-order convergent. Once we move outside this finest region, however, convergence drops down precipitously. We note, however, that the momentum constraint in general is 2 to 3 orders of magnitude lower than the
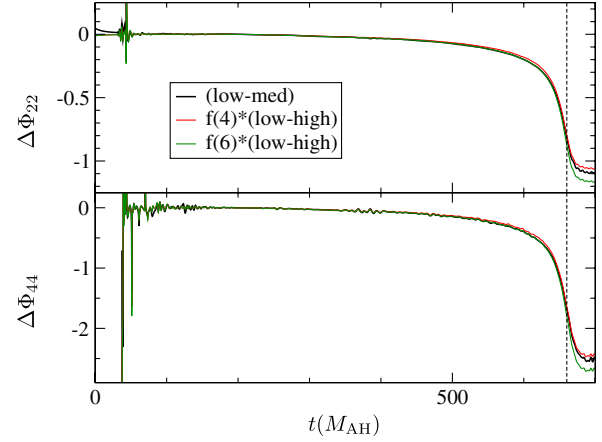

FIG. 17 (color online). Phase convergence for the (2, 2) (upper panel) and (4, 4) (lower panel) modes of the X1UD simulations, based on the central resolutions $M/96$, $M/128$, and $M/160$. In each case, the $(M/96 - M/160)$ difference has been scaled up assuming fourth- and sixth-order convergence. The phase differences appear to be consistent with sixth-order convergence through late inspiral, declining to closer to fifth order at merger and ringdown.

Hamiltonian constraint, which suggests that there is a small amount of low-order error present in all constraints, but which is dominated by higher-amplitude (but convergent) error only in the Hamiltonian constraint.

Constraint violation information was not available for the Cactus-based X400 simulations.

2. Waveforms

In Figs. 14 and 15, we demonstrate sixth-order convergence for the (2, 2) and (4, 4) modes' amplitudes and phases, respectively.

For the 4:1 data (Fig. 16), we see generally cleaner waveforms, but also a large oscillation in errors until about $400M$ into the evolution. After this, convergence appears to be sixth order until close to amplitude peak time, when it declines to fourth order. This may be because the overall error is dominated by uncertainties in the merger time, which is determined by the fourth-order-accurate Runge-Kutta time-integration scheme. Unfortunately, we could not disentangle this effect to sufficient accuracy to establish sixth-order convergence through the peak time.

The 4:1 waveform phase evolution (Fig. 17) also seems to display sixth-order convergence until the merger, when it declines to fifth order. We note that the scale of the errors is generally less than half those of the X1UD data from Fig. 15.

[1] F. Pretorius, Phys. Rev. Lett. **95,** 121101 (2005).

[2] F. Pretorius, Classical Quantum Gravity **23,** S529 (2006).

[3] J. G. Baker, J. M. Centrella, D.-I. Choi, M. Koppitz, and J. R. van Meter, Phys. Rev. Lett. **96,** 111102 (2006).

[4] M. Campanelli, C. O. Lousto, P. Marronetti, and Y. Zlochower, Phys. Rev. Lett. **96,** 111101 (2006).

[5] J. G. Baker, J. M. Centrella, D.-I. Choi, M. Koppitz, and J. R. van Meter, Phys. Rev. D **73,** 104002 (2006).

[6] J. G. Baker, M. Campanelli, F. Pretorius, and Y. Zlochower, Classical Quantum Gravity **24,** S25 (2007).

[7] M. D. Hannam, S. Husa, J. G. Baker, M. Boyle, B. Brügmann, T. Chu, E. N. Dorband, F. Herrmann, I. Hinder, B. J. Kelly *et al.*, Phys. Rev. D **79,** 084025 (2009).

[8] J. G. Baker, W. D. Boggs, J. M. Centrella, B. J. Kelly, S. T. McWilliams, and J. R. van Meter, Phys. Rev. D **78,** 044046 (2008).

[9] A. Buonanno, Y. Pan, J. G. Baker, J. M. Centrella, B. J. Kelly, S. T. McWilliams, and J. R. van Meter, Phys. Rev. D **76,** 104049 (2007).

[10] A. Buonanno, Y. Pan, H. P. Pfeiffer, M. A. Scheel, L. T. Buchman, and L. E. Kidder, Phys. Rev. D **79,** 124028 (2009).

[11] C. R. Galley, F. Herrmann, J. Silberholz, M. Tiglio, and G. Guerberoff, Classical Quantum Gravity **27,** 245007 (2010).

[12] M. Campanelli, C. O. Lousto, and Y. Zlochower, Phys. Rev. D **74,** 041501(R) (2006).

[13] D. M. Shoemaker, B. Vaishnav, I. Hinder, and F. Herrmann, Classical Quantum Gravity **25,** 114047 (2008).

[14] C. Reisswig, S. Husa, L. Rezzolla, E. N. Dorband, D. Pollney, and J. Seiler, Phys. Rev. D **80,** 124026 (2009).

[15] T. Chu, H. P. Pfeiffer, and M. A. Scheel, Phys. Rev. D **80,** 124051 (2009).

[16] P. Mösta, C. Palenzuela, L. Rezzolla, L. Lehner, S. Yoshida, and D. Pollney, Phys. Rev. D **81,** 064017 (2010).

[17] M. D. Hannam, S. Husa, F. Ohme, D. Müller, and B. Brügmann, Phys. Rev. D **82,** 124008 (2010).

[18] P. Ajith, M. D. Hannam, S. Husa, Y. Chen, B. Brügmann, E. N. Dorband, D. Müller, F. Ohme, D. Pollney, C. Reisswig *et al.*, Phys. Rev. Lett. **106,** 241101 (2011).

[19] L. Santamaría, F. Ohme, P. Ajith, B. Brügmann, E. N. Dorband, M. D. Hannam, S. Husa, P. Mösta, D. Pollney, C. Reisswig *et al.*, Phys. Rev. D **82,** 064016 (2010).

[20] R. Sturani, S. Fischetti, L. Cadonati, G. M. Giudi, J. Healy, D. M. Shoemaker, and A. Viceré, arXiv:1010.5172.

[21] R. Sturani, S. Fischetti, L. Cadonati, G. M. Giudi, J. Healy, D. M. Shoemaker, and A. Viceré, J. Phys. Conf. Ser. **243,** 012007 (2010).

[22] S. Husa, M. D. Hannam, J. A. González, U. Sperhake, and B. Brügmann, Phys. Rev. D **77,** 044037 (2008).

[23] M. Campanelli, C. O. Lousto, H. Nakano, and Y. Zlochower, Phys. Rev. D **79,** 084010 (2009).

[24] A. Buonanno, Y. Chen, and T. Damour, Phys. Rev. D **74,** 104005 (2006).

[25] T. Damour, P. Jaranowski, and G. Schäfer, Phys. Rev. D **77,** 064032 (2008).

[26] R. A. Porto and I. Z. Rothstein, Phys. Rev. Lett. **97,** 021101 (2006).

[27] J. Steinhoff, S. Hergt, and G. Schäfer, Phys. Rev. D **77,** 081501(R) (2008).

[28] J. Steinhoff, S. Hergt, and G. Schäfer, Phys. Rev. D **78,** 101503(R) (2008).

[29] R. A. Porto and I. Z. Rothstein, arXiv:0712.2032.

[30] S. Hergt, J. Steinhoff, and G. Schäfer, Classical Quantum Gravity **27,** 135007 (2010).

[31] L. Blanchet, A. Buonanno, and G. Faye, Phys. Rev. D **74,** 104034 (2006); **75,** 049903(E) (2007); **81,** 089901(E) (2010).

[32] B. Imbiriba, J. G. Baker, D.-I. Choi, J. M. Centrella, D. R. Fiske, J. D. Brown, J. R. van Meter, and K. M. Olson, Phys. Rev. D **70,** 124025 (2004).

[33] P. MacNeice, K. M. Olson, C. Mobarry, R. de Fainchtein, and C. Packer, Comput. Phys. Commun. **126,** 330 (2000).

[34] Einstein Toolkit, http:einsteintoolkit.org.

[35] Cactus Computational Toolkit, http://www .cactuscode.org.

[36] Carpet: Adaptive Mesh Refinement for the Cactus Framework, http://www.carpetcode.org/.

[37] S. R. Brandt and B. Brügmann, Phys. Rev. Lett. **78,** 3606 (1997).

[38] J. M. Bowen and J. W. York, Jr., Phys. Rev. D **21,** 2047 (1980).

[39] M. Ansorg, B. Brügmann, and W. Tichy, Phys. Rev. D **70,** 064011 (2004).

[40] R. J. Gleiser, C. O. Nicasio, R. H. Price, and J. A. Pullin, Phys. Rev. D **57,** 3401 (1998).

[41] M. Campanelli, B. J. Kelly, and C. O. Lousto, Phys. Rev. D **73,** 064005 (2006).

[42] D.-I. Choi, B. J. Kelly, W. D. Boggs, J. G. Baker, J. M. Centrella, and J. R. van Meter, Phys. Rev. D **76,** 104026 (2007).

[43] T. Nakamura, K. Oohara, and Y. Kojima, Prog. Theor. Phys. Suppl. **90,** 1 (1987).

[44] M. Shibata and T. Nakamura, Phys. Rev. D **52,** 5428 (1995).

[45] T. W. Baumgarte and S. L. Shapiro, Phys. Rev. D **59,** 024007 (1998).

[46] J. R. van Meter, ''From Geometry to Numerics'' (Institut Henri Poincaré, Paris, 2006), http://luth2.obspm.fr/IHP06/ workshops/geomnum/slides/vanmeter.pdf.

[47] W. Tichy and P. Marronetti, Phys. Rev. D **76,** 061502(R) (2007).

[48] P. Marronetti, W. Tichy, B. Brügmann, J. A. González, and U. Sperhake, Phys. Rev. D **77,** 064010 (2008).

[49] M. D. Duez, S. L. Shapiro, and H.-J. Yo, Phys. Rev. D **69,** 104016 (2004).

[50] H.-O. Kreiss and J. Oliger, *Methods for Approximate Solution of Time Dependent Problems*, GARP Publications Series Vol. 10 (World Meteorological Organization and International Council of Scientific Unions, Geneva, 1973).

[51] P. Hübner, Classical Quantum Gravity **16,** 2823 (1999).

[52] J. R. van Meter, J. G. Baker, M. Koppitz, and D.-I. Choi, Phys. Rev. D **73,** 124011 (2006).

[53] J. Thornburg, AIP Conf. Proc. **686,** 247 (2003).

[54] J. Thornburg, Classical Quantum Gravity **21,** 743 (2004).

[55] D. Christodoulou, Phys. Rev. Lett. **25,** 1596 (1970).

[56] J. G. Baker, S. T. McWilliams, J. R. van Meter, J. M. Centrella, D.-I. Choi, B. J. Kelly, and M. Koppitz, Phys. Rev. D **75,** 124024 (2007).

[57] J. G. Baker, M. Campanelli, and C. O. Lousto, Phys. Rev. D **65**, 044001 (2002).
[58] C. W. Misner, K. S. Thorne, and J. A. Wheeler, *Gravitation* (Freeman, San Francisco, 1973).
[59] C. Reisswig and D. Pollney, Classical Quantum Gravity **28**, 195015 (2011).
[60] C. O. Lousto and Y. Zlochower, Phys. Rev. D **76**, 041502 (R) (2007).
[61] M. Ruiz, M. Alcubierre, D. Nuñez, and R. Takahashi, Gen. Relativ. Gravit. **40**, 1705 (2007); **40**, 2467(E) (2008).
[62] L. M. Burko and S. A. Hughes, Phys. Rev. D **82**, 104029 (2010).
[63] J. G. Baker, B. J. Kelly, and J. R. van Meter (unpublished).
[64] E. Barausse and L. Rezzolla, Astrophys. J. **704**, L40 (2009).
[65] L. Rezzolla, P. Diener, E. N. Dorband, D. Pollney, C. Reisswig, E. Schnetter, and J. Seiler, Astrophys. J. **674**, L29 (2008).
[66] W. Tichy and P. Marronetti, Phys. Rev. D **78**, 081501(R) (2008).
[67] C. O. Lousto, M. Campanelli, and Y. Zlochower, Classical Quantum Gravity **27**, 114006 (2010).
[68] L. Rezzolla, E. Barausse, E. N. Dorband, D. Pollney, C. Reisswig, J. Seiler, and S. Husa, Phys. Rev. D **78**, 044002 (2008).
[69] L. E. Kidder, Phys. Rev. D **77**, 044016 (2008).
[70] S. L. Detweiler, Astrophys. J. **239**, 292 (1980).
[71] E. Berti, V. Cardoso, and A. O. Starinets, Classical Quantum Gravity **26**, 163001 (2009).
[72] A. Buonanno, G. B. Cook, and F. Pretorius, Phys. Rev. D **75**, 124018 (2007).
[73] Y. Pan, A. Buonanno, M. Boyle, L. T. Buchman, L. E. Kidder, H. P. Pfeiffer, and M. A. Scheel, arXiv:1106.1021.
[74] S. A. Teukolsky, Astrophys. J. **185**, 635 (1973).
[75] Advanced LIGO, http://www.ligo.caltech.edu/advLIGO/.
[76] B. J. Owen, Phys. Rev. D **53**, 6749 (1996).
[77] C. Cutler and E. E. Flanagan, Phys. Rev. D **49**, 2658 (1994).
[78] LSC-Virgo Data Analysis Working Groups, LSC-Virgo White Paper on Gravitational Wave Data Analysis, Report Nos. LIGO-T080278-00-Z, VIR-095A-08, http://www.ligo.caltech.edu/docs/T/T080278-00.pdf.
[79] L. M. Goggin, °Ph.D. thesis, California Institute of Technology, 2008.
[80] L. Cadonati, S. Chatterji, S. Fischetti, G. Guidi, S. R. P. Mohapatra, R. Sturani, and A. Viceré, Classical Quantum Gravity **26**, 204005 (2009).10.1088/0264-9381/26/20/204005
[81] A. S. Sengupta, J. Phys. Conf. Ser. **228**, 012002 (2010).10.1088/1742-6596/228/1/012002
[82] Y. Pan, A. Buonanno, J. G. Baker, J. M. Centrella, B. J. Kelly, S. T. McWilliams, F. Pretorius, and J. R. van Meter, Phys. Rev. D **77**, 024014 (2008).10.1103/PhysRevD.77.024014
[83] Y. Pan, A. Buonanno, L. T. Buchman, T. Chu, L. E. Kidder, H. P. Pfeiffer, and M. A. Scheel, Phys. Rev. D **81**, 084041 (2010).10.1103/PhysRevD.81.084041
[84] Y. Pan, A. Buonanno, R. Fujita, E. Racine, and H. Tagoshi, Phys. Rev. D **83**, 064003 (2011).10.1103/PhysRevD.83.064003